

# Scaling laws and multi-scale approach in the mechanics of heterogeneous and disordered materials

Alberto Carpinteri\*, Pietro Cornetti, Simone Puzzi

Politecnico di Torino  
Department of Structural and Geotechnical Engineering, Torino, Italy

## Contents

<b>1</b>	<b>Introduction</b>	<b>1</b>
<b>2</b>	<b>The nonlinear model</b>	<b>3</b>
2.1	The dimensional analysis approach . . . . .	3
2.1.1	Dimensional analysis and renormalization group theory . . . . .	3
2.1.2	Application of the Dimensional Analysis to the beam model . . . . .	4
2.1.3	Virtual propagation of brittle fracture . . . . .	4
2.2	Basic concepts of the cohesive crack model	5
2.2.1	Cohesive interpretation of the beam model . . . . .	6
2.3	Mode I problems . . . . .	7
2.3.1	Numerical implementation . . . . .	7
2.3.2	Numerical simulations . . . . .	8
<b>3</b>	<b>The fractal model</b>	<b>10</b>
3.1	The effect of the microstructural disorder	10
3.1.1	The fractal approach . . . . .	10
3.1.2	Scale-independent cohesive crack model . . . . .	12
3.2	Local fractional calculus and fractal functions . . . . .	14
3.2.1	Size effects on tensile and flexural strength . . . . .	16
3.2.2	The fractal bar . . . . .	17
3.3	Multifractal scaling laws . . . . .	17
	<b>References</b>	<b>19</b>

## Abstract

*The present paper is a review of the research works carried out on scaling laws and multi-scaling approach in the mechanics of heterogeneous and disordered materials at the Politecnico di Torino during the last two decades. The subject encompasses theoretical, numerical and experimental aspects.*

\*corresponding author: alberto.carpinteri@polito.it, tel. +390115644850, fax +390115644899

*The research work followed two main directions. The first one concerns the implementation and the development of the cohesive crack model, which has been shown to be able to simulate experiments on concrete-like materials and structures. It is referred to as the dimensional analysis approach, since it succeeds in capturing the ductile-to-brittle transition by increasing the structural size owing to the different physical dimensions of two material parameters: the tensile strength and the fracture energy.*

*The second research direction aims at capturing the size-scale effects of quasi-brittle materials, which show fractal patterns in the failure process. This approach is referred to as the renormalization group (or fractal) approach and leads to a scale-invariant fractal cohesive crack model. This model is able to predict the size effects even in tests where the classical approach fails, e.g. the direct tension test. Within this framework and introducing the fractional calculus, it will be shown how the Principle of Virtual Work can be rewritten in its fractional form, thus obtaining a scaling law not only for the tensile strength and the fracture energy, but also for the critical strain.*

## 1 Introduction

Several physical phenomena can be analysed through Continuum Mechanics whenever only one length or energy scale is relevant, namely the macroscopic scale. When a critical phenomenon is imminent, also other scales of observation become relevant, as, for instance, in phase transformations, laminar to turbulent flow transitions, laser light formation, superconductivity, material failure, etc. These are co-operative and multiscale phenomena, where the global behaviour cannot be predicted simply by applying a local law. In other words, the system is to be considered complex with a hierarchy of scales of observation and the corresponding specific phenomena occurring at those scales (Wilson [1], Herrmann and Roux [2]). Usually, a rather rough distinction between micro-, meso-, and macroscopic scales is made, although the scaling range is in actual fact continuous and not discrete. In practice, the observer can pass from one observation scale to another without any discontinuity.

*Material damage, strain localisation, and fracture* are phenomena not always interpretable in the framework of Continuum Mechanics. While Fracture Mechanics represents a first departure from the classical continuum theories, where regular and differentiable functions are implicitly assumed, it is not always suitable to simulate and justify the scaling laws emerging from experimental tests. In particular, it is difficult to explain the size effects on tensile strength and fracture energy, when purely tensile tests on initially uncracked specimens are considered.

Up to the present century, the strength of materials has always been considered as independent of specimen size. The concept that a rope with cross-sectional area twice that of another rope of the same material can sustain a load twice that sustainable by the thinner rope was already proposed by Leonardo da Vinci in his "Codice Atlantico", and by Galileo Galilei in his "Discorsi intorno a due Nuove Scienze". Of course this is true, at least approximately. On the other hand, can such an assumption be extrapolated to very different sizes, where the scaling range may be one or even several orders of magnitude? And, again, can such an assumption be extended also to sizes for which the material must be considered heterogeneous and disordered?

In the last century, these questions have met with a number of negative answers, which, to use Popperian terms [3], represent confutations of the former *conjecture* that strength is a constant and scale-invariant material property. From the hulls of the Liberty Ships, which broke at very low stresses, to glass filaments (*whiskers*), which break only under very high stresses, many are the examples provided by modern technology that lead to the surprising conclusion that material strength decreases with body size.

Many cases of strength size-dependence have been pointed out by scientists and engineers. Those already mentioned of glass filaments and ships hulls are the best known and lie at either extreme of the size scale. Many other cases at a laboratory size-scale have been treated and commented upon, and in some cases interpreted, by various Authors of different generations (Carpinteri [4]).

There are many different approaches to explain this size-scale effect.

In the framework of Fracture Mechanics the most recurrent explanations are based on Dimensional Analysis and on the dimension mismatch between the two quantities governing the material behaviour, namely the yield strength  $\sigma_y$ , whose dimensions are  $[F][L]^{-2}$ , and the fracture toughness  $K_{IC}$ , whose dimensions are  $[F][L]^{-3/2}$ . Through the application of the Buckingham's II theorem, it is possible to define the true nondimensional quantity determining the failure behaviour of the considered system, i.e. the brittleness number  $s_E$ .

Dimensional Analysis can be applied to classical LEFM models, like the beam model, as well to nonlinear fracture mechanics models, like the cohesive crack. Applications of both models to bending geometry will be considered in the first section of the paper.

Starting in the 1990's, the research frontier of Material Strength considered the novel concepts of disorder, fractality, and renormalisation group, in order to describe the ductile-to-brittle transition and the size-scale effects in a unified manner.

Fractals are geometrical sets with the following two properties (Feder [5], Mandelbrot [6], Falconer [7]):

1. *Self similarity*, i.e. they present the same shape or features at every scale. This property can be extended to statistical features (random fractals).
2. *Non-integer dimension*, i.e. they present a dimension larger (invasive fractals) or smaller (lacunar fractals) than that of the classical reference domain.

The fractal dimension can be considered as a measure of the geometrical disorder of the system. Examples of natural fractals with dimension comprised between 1 and 2 are mountain outlines, cloud contours, coastline profiles, river patterns, streaks of lightning, snow-flakes, arterial systems, and the lunar surface (craters excluded). Natural fractals with dimension comprised between 2 and 3 are for example: diffusion fronts, sponge cloths, foams, brain folds, and mass distribution in the universe. It is interesting to note that, whereas the lunar surface and sponge cloths are lacunar fractals in relation to surfaces and volumes, respectively, coastline profiles and diffusion fronts are instead invasive fractals in relation to one-dimensional and two-dimensional loci, respectively.

Also *fracture surfaces* (after rupture) may be considered invasive fractals of a dimension comprised between 2 and 3, as demonstrated by Mandelbrot et al. [8] for metallic materials, and by Saouma et al. [9] for cementitious materials. An additional assumption may be that of considering material ligaments (at peak stress) as lacunar fractals of a dimension comprised between 1 and 2 (see Carpinteri [10, 11], Carpinteri and Ferro [12], Carpinteri et al. [13]).

If the experimental investigation is carried out over more than one order of magnitude in the scaling range, it is clear how not only a single and unique fractal dimension of fracture surface (Carpinteri and Chiaia [14], Carpinteri et al. [15]) or material ligament may be measured by varying the structural scale. This apparent anomaly is in fact due to the different fractal character which emerges at the different scales. In nature there are no ideal geometrical fractals; natural morphologies are generally *random multifractals* due to the limited size of the heterogeneities or perturbations (e.g., concrete aggregates). Whereas ideal fractals do not present any characteristic length, for random multifractals it is possible to distinguish between small scales, at which disorder prevails, and large scales, at which order prevails. For fracture surfaces, the microscopic disorder is that of *Brownian* surfaces with fractal dimension equal to 2.5, whereas the macroscopic order is that of *Euclidean* surfaces, with integer dimension equal to 2. On the other hand, for material ligaments at peak stress, the microscopic disorder

is that of a lacunar surface with fractal dimension equal to 1.5, whereas the macroscopic order is that of a classical cross-sectional plane with integer dimension equal to 2.

In the framework of this global fractal view, when the scale of observation tends to zero, the nominal tensile strength tends to infinity, whereas the nominal fracture energy tends to zero. In this way, it is possible to interpret the very high strength values found by Griffith [16] for glass filaments as well as the initial part of the J-Resistance Curve (Begley and Landes [17]). On the other hand, when the scale of observation tends to infinity, the nominal tensile strength tends to a lower limit, just as the nominal fracture energy tends to an upper limit. These trends represent very realistically the low failure stresses of the Liberty ships and the plateau of the J-Resistance Curve [17] respectively.

## 2 The nonlinear model

### 2.1 The dimensional analysis approach

This first section of the paper is devoted to a brief review of the fundamentals of Dimensional Analysis and of the Cohesive Crack model, along with some examples for structures in bending, namely, the beam model, and numerical implementations for Mode I cracking. It will be shown how this approach succeeds in capturing the ductile to brittle transition by increasing the structural size owing to the difference in the physical dimensions of two materials parameters: the tensile strength  $\sigma_y$  and the fracture toughness  $K_{IC}$ .

#### 2.1.1 Dimensional analysis and renormalization group theory

The scaling law for strength (or toughness) of disordered materials may be regarded as a particular case of *complete similarity*, through the application of Dimensional Analysis and Buckingham's  $\Pi$  Theorem [18].

Let  $q_0$  be the peak load for a cracked body. This load is a function of a number of variables:

$$q_0 = F(q_1, q_2, \dots, q_n; r_1, r_2, \dots, r_m) \quad (1)$$

where  $q_i$  are physical quantities with different dimensions and  $r_i$  are nondimensional numbers. Let us consider two dimensionally independent quantities  $q_1$  and  $q_2$  so that the product  $q_1^{\alpha_{10}} q_2^{\alpha_{20}}$  has the same dimensions as  $q_0$  for suitable values of  $\alpha_{10}$  and  $\alpha_{20}$ . In the same way, the product  $q_1^{\alpha_{13}} q_2^{\alpha_{23}}$  can have the same dimensions as  $q_3$  for suitable values of  $\alpha_{13}$  and  $\alpha_{23}$ , and so on. Function (1) can therefore be transformed into (Carpinteri [19, 20]):

$$\frac{q_0}{q_1^{\alpha_{10}} q_2^{\alpha_{20}}} = \Pi \left( \frac{q_3}{q_1^{\alpha_{13}} q_2^{\alpha_{23}}}, \frac{q_4}{q_1^{\alpha_{14}} q_2^{\alpha_{24}}}, \dots, \frac{q_n}{q_1^{\alpha_{1n}} q_2^{\alpha_{2n}}}; r_1, r_2, \dots, r_m \right) \quad (2)$$

or

$$\Pi_0 = \Pi(\Pi_3, \Pi_4, \dots, \Pi_n; r_1, r_2, \dots, r_m) \quad (3)$$

In the simple case of elastic-perfectly plastic material and three-point bending test geometry, Eq. (3) is given by

$$\frac{F}{\sigma_y b^2} = \Pi \left( \frac{\mathcal{G}_{IC}}{\sigma_y b}; \frac{a_0}{b}, \frac{l}{b}, \frac{t}{b} \right) \quad (4)$$

where  $\sigma_y$  is the yield strength and  $\mathcal{G}_{IC}$  the fracture energy of the material;  $b$  is the beam depth (reference size), while  $l$  and  $t$  are the span and thickness of the beam, respectively, and  $a_0$  is the initial crack depth. Expression (4) represents the generalised homogeneity of the function  $F$  in Eq. (1), and therefore a case of *complete similarity*, governed by Dimensional Analysis. The strength and toughness parameters,  $\sigma_y$  and  $\mathcal{G}_{IC}$  are defined in the traditional way, as material constants. A scale interaction between the related phenomena (plastic collapse and brittle fracture, respectively) is ruled by the brittleness number  $s_E = \mathcal{G}_{IC}/\sigma_y b$  (Carpinteri [4, 21, 22, 23]).

On the other hand, some of the dimensionless parameters in Eq. (4) can tend to zero or to infinity. For instance, when the crack depth  $a$  tends to zero, the material and the other specimen sizes remaining unchanged, we have

$$\lim_{\alpha \rightarrow 0} \frac{F}{\sigma_y b^2} = \lim_{\alpha \rightarrow 0} \Pi(s_E; \alpha, \lambda, \tau) = \frac{\tau}{\lambda} \quad (5)$$

where the Greek letters represent the corresponding nondimensional quantities. In other words, there exists a limit of the function  $\Pi$  which is finite and different from zero, so that  $\Pi$  can be replaced trivially by a simpler function.

When the specimen size  $b$  tends to zero, the material and the specimen shape remaining unchanged, it is found by experiment that

$$\lim_{b \rightarrow 0} \frac{F}{\sigma_y b^2} = \lim_{b \rightarrow 0} \Pi(s_E; \alpha, \lambda, \tau) \neq \Pi(\infty; \alpha, \lambda, \tau), \quad (6)$$

i.e.  $\neq (1 - \alpha)^2 \frac{\tau}{\lambda}$

In actual fact, ever since Griffith's pioneering paper, we know that, when  $b \rightarrow 0$ ,  $F/b \rightarrow \infty$ , as does  $b^{-1/2}$  Eq. (6) should therefore be substituted by

$$\lim_{b \rightarrow 0} \frac{F}{\sigma_y b^2} = s_E^{1/2} \lim_{b \rightarrow 0} \bar{\Pi} \left( \frac{\alpha}{s_E^{\beta_2}}, \frac{\lambda}{s_E^{\beta_3}}, \frac{\tau}{s_E^{\beta_4}} \right) \quad (7)$$

and Eq. (4) by

$$\frac{F}{\sigma_y b^2} = s_E^{1/2} \bar{\bar{\Pi}} \left( \frac{\alpha}{s_E^{\beta_2}}, \frac{\lambda}{s_E^{\beta_3}}, \frac{\tau}{s_E^{\beta_4}} \right) \quad (8)$$

Expression (8) represents the generalised homogeneity of the function  $\Pi$  Eq. (4), and therefore a case of *incomplete similarity* (Barenblatt [24]) governed by Renormalisation Group Theory. The strength and toughness parameters,

$\sigma_y$  and  $\mathcal{G}_{IC}$ , prove not to be experimental material constants. They become scale-independent constants only if anomalous physical dimensions are assumed. A direct scale interaction between the parameters themselves emerges, with a total convergence of roles (at least at the microscopic scale). If  $W$  represents the energy dissipated in the failure process, it is then possible to write an expression analogous to Eq. (8)

$$\frac{W}{\sigma_y b^2} = s_E^{1/2} \bar{\Pi} \left( \frac{\alpha}{s_E^{\gamma_2}}, \frac{\lambda}{s_E^{\gamma_3}}, \frac{\tau}{s_E^{\gamma_4}} \right) \quad (9)$$

In the following section, Dimensional Analysis will be applied to a fracture mechanics based model, the beam model. As it will be seen, this approach is able to capture the *ductile-brittle* transition through the definition of a *Brittleness* number  $s$ .

### 2.1.2 Application of the Dimensional Analysis to the beam model

Due to the different physical dimensions of ultimate tensile strength,  $\sigma_u$ , and fracture toughness,  $K_{IC}$ , scale effects are always present in the usual fracture testing of common engineering materials. This means that, for the usual size-scale of the laboratory specimens, the ultimate strength collapse or the plastic collapse at the ligament tends to anticipate and obscure the brittle crack propagation. Such a competition between collapses of a different nature can easily be shown by considering the ASTM formula [25] for the three point bending test evaluation of fracture toughness (Fig. 1):

$$K_I = \frac{Pl}{th^{3/2}} f\left(\frac{a_0}{h}\right) \quad (10)$$

with

$$f\left(\frac{a_0}{h}\right) = 2.9 \left(\frac{a}{h}\right)^{1/2} - 4.6 \left(\frac{a}{h}\right)^{3/2} + 21.8 \left(\frac{a}{h}\right)^{5/2} - 37.6 \left(\frac{a}{h}\right)^{7/2} + 38.7 \left(\frac{a}{h}\right)^{9/2} \quad (11)$$

At the crack propagation Eq. (10) becomes:

$$K_{IC} = \frac{P_{\max} l}{th^{3/2}} f\left(\frac{a_0}{h}\right) \quad (12)$$

where  $P_{\max}$  is the external load of brittle fracture. If both members of Eq. (12) are divided by  $\sigma_u b^{1/2}$  we obtain:

$$\frac{K_{IC}}{\sigma_u h^{1/2}} = s = \frac{P_{\max} l}{\sigma_u t h^2} f\left(\frac{a}{h}\right) \quad (13)$$

where  $s$  is the brittleness number defined by Carpinteri [4, 19–23, 26, 27]. Rearranging of Eq. (13) gives:

$$\frac{P_{\max} l}{\sigma_u t h^2} = \frac{s}{f\left(\frac{a}{h}\right)} \quad (14)$$

On the other hand, it is possible to consider the non-dimensional load of ultimate strength in a beam of depth  $(h - a)$ :

$$\frac{P_{\max} l}{\sigma_u t h^2} = \frac{2}{3} \left(1 - \frac{a}{h}\right)^2 \quad (15)$$

Equations (14) and (15) are plotted in Fig. 1 as functions of the track depth  $a/h$ . While the former produces a set of curves by varying the brittleness number  $s$ , the latter is represented by a unique curve. It is evident that the ultimate strength collapse at the ligament precedes crack propagation for each initial crack depth, when the brittleness number  $s$  is higher than the limit-value  $s_0 = 0.50$ .

For lower  $s$  numbers, ultimate strength collapse anticipates crack propagation only for crack depths external to a certain interval. This means that a true LEFM collapse occurs only for comparatively low fracture toughnesses, high tensile strengths and/or large structure sizes. Not the single values of  $K_{IC}$ ,  $\sigma_u$  and  $h$  determine the nature of the collapse, but only their function  $s$  does, see Eq. (13).

### 2.1.3 Virtual propagation of brittle fracture

The flexural behaviour of the beam in Fig. 1 will be analyzed. The deflection due to the elastic compliance of the uncracked beam is:

$$\delta_e = \frac{Pl^3}{48EI} \quad (16)$$

where  $I$  is the inertial moment of the cross-section. On the other hand, the deflection due to the local crack compliance is (Tada et al. [28]):

$$\delta_c = \frac{3}{2} \frac{Pl^2}{t h^2 E} g\left(\frac{a}{h}\right) \quad (17)$$

with:

$$g\left(\frac{a}{h}\right) = \left(\frac{\frac{a}{h}}{1 - \frac{a_0}{h}}\right) \left[ 5.58 - 19.57 \left(\frac{a}{h}\right) + 36.82 \left(\frac{a}{h}\right)^2 - 34.94 \left(\frac{a}{h}\right)^3 + 12.77 \left(\frac{a}{h}\right)^4 \right] \quad (18)$$

The superposition principle provides:

$$\delta = \delta_e + \delta_c \quad (19)$$

and, in non-dimensional form:

$$\frac{\delta l}{\varepsilon_u h^2} = \frac{Pl}{\sigma_u t h^2} \left[ \frac{1}{4} \left(\frac{l}{h}\right)^3 + \frac{3}{2} \left(\frac{l}{h}\right)^2 g\left(\frac{a}{h}\right) \right] \quad (20)$$

where  $\varepsilon_u = \sigma_u/E$ . The term within square brackets is the dimensionless compliance, which is a function of the beam slenderness,  $l/h$ , as well as of the crack depth,  $a/h$ . Some linear load-deflection diagrams are represented in Fig. 2, by varying the crack depth  $a/h$  and for the fixed ratio  $l/h = 4$ .

Through Eqs. (14) and (15), it is possible to determine the point of crack propagation as well as the point of ultimate strength on each linear plot in Fig. 2. Whereas the former depends on the brittleness number  $s$ , the latter is unique. The set of the crack propagation points with  $s = \text{constant}$  and by varying the crack depth, represents a virtual load-deflection path, where point by point the load is always that producing crack instability.

When the crack grows, the load of instability decreases and the compliance increases, so that the product at the right member of Eq. (20) may result to be either decreasing or increasing. The diagrams in Fig. 2 show the deflection decreasing (with the load) up to the crack depth  $a/h \simeq 0.3$  and then increasing (in discordance with the load). Therefore, whereas for  $a/h > 0.3$  the  $P - \delta$  curve presents the usual softening course with negative derivative, for  $a/h < 0.3$  it presents positive derivative. Such a branch could not be revealed by deflection controlled testing and the representative point would jump from the positive to the negative branch with a behaviour discontinuity.

The set of the ultimate strength points, by varying the crack depth, is represented by the thick line in Fig. 2. Such a line intersects the virtual crack propagation curves with  $s \leq s_0 = 0.50$ , analogous to what was shown in Fig. 1, and presents a slight indentation with  $dP/d\delta > 0$ . The crack mouth opening displacement  $w$  is a function of the specimen geometry and of the elastic modulus (Tada et al. [28]):

$$w_1 = \frac{6Pla}{th^2E} m\left(\frac{a}{h}\right) \quad (21)$$

with:

$$m\left(\frac{a}{h}\right) = 0.76 - 2.28\left(\frac{a}{h}\right) + 3.87\left(\frac{a}{h}\right)^2 - 2.04\left(\frac{a}{h}\right)^3 + \frac{0.66}{(1 - a/h)^2} \quad (22)$$

In non-dimensional form Eq.(21) becomes:

$$\frac{w_1 l}{\varepsilon_u h^2} = \frac{Pl}{\sigma_u t h^2} \left[ 6\left(\frac{l}{h}\right) \left(\frac{a}{h}\right) m\left(\frac{a}{h}\right) \right] \quad (23)$$

The term within square brackets is the dimensionless compliance which, also in this case, depends on beam slenderness and crack depth. Some linear load-crack mouth opening displacement diagrams are reported in Fig. 3, by varying the crack depth  $a/h$  and for  $l/h = 4$ .

## 2.2 Basic concepts of the cohesive crack model

The Cohesive Crack Model was initially proposed by Barenblatt [29, 30] and Dugdale [31]. Subsequently, Dugdale's model was reconsidered by Bilby et al. [32], Rice [33], Willis [34], and utilized by Wnuk [35], who referred to it as the Final Stretch criterion. Hillerborg et al. [36] proposed the Fictitious Crack Model in order to study crack propagation in concrete. The cohesive crack

model is based on the following assumptions (Carpinteri [21], Hillerborg et al. [36], Carpinteri et al. [37]):

1. The cohesive fracture zone (plastic or process zone) begins to develop when the maximum principal stress achieves the ultimate tensile strength  $\sigma_u$  (Fig. 4).
2. The material in the process zone is partially damaged but still able to transfer stress. Such a stress is dependent on the crack opening displacement  $w$  (Fig. 4).

The energy necessary to produce a unit crack surface is given by the area under the  $\sigma - w$  diagram in Fig. 4:

$$\mathcal{G}_F = \int_0^{w_c} \sigma dw = \frac{1}{2} \sigma_u w_c \quad (24)$$

The *real crack tip* is defined as the point where the distance between the crack surfaces is equal to the critical value of crack opening displacement  $w_c$  and the normal stress vanishes. On the other hand, the *fictitious crack tip* is defined as the point where the normal stress attains the maximum value and the crack opening vanishes (Fig. 4).

There are some similarities among Barenblatt's, Dugdale's, Rice's and Hillerborg's formulations: the crack tip faces close smoothly (the stress intensity factor  $K_I$  vanishes at the crack tip) and the fracture process zone is of negligible thickness. On the other hand, the closing stresses in the fracture process zone are constant only in Dugdale's model, while the size of this zone is constant and small in comparison with the length of the main crack only in Barenblatt's model.

With some modifications, the cohesive crack model has been applied to model a wide range of materials and fracture mechanisms, most prominently concrete. Regarding this material, there is a very large literature; after Hillerborg et al. [36] and Petterson [38], the fictitious crack model was further applied by Wecharatana and Shah [39], Bažant and Oh [40] and Ingraffea and Gerstle [41]. More recently, the former terminology of Cohesive Crack Model has been reproposeed by Carpinteri [4, 21, 23, 42], Carpinteri et al. [37, 43, 44] and the model has been used with this terminology by a number of researchers (for instance, Carpinteri and Valente [45], Cen and Maier [46], Elices et al. [47], among others). Developments in this area have been described by Elices et al. [48], Planas et al. [49] and Bažant [50]. A comprehensive overview of concrete structures analyzed by means of the cohesive model is given by Carpinteri and Ferro [51]. However, the cohesive model has been applied successfully to model different materials, such as polymers; Tijssens [52] modelled materials with hard aggregates in a visco-plastic matrix, whilst Tijssens et al. [53] addressed the craze formation in polymers. Regarding metals, very fundamental work on this subject was performed by Needleman [54, 55], Tvergaard and Hutchinson [56–58], and Tvergaard [59]. Further work on crack extension in metallic materials has

been published by Lin [60] and Lin et al. [61, 62]. Recently, several issues were also addressed by means of the Cohesive Crack Model, e.g. dynamic fracture (Xu and Needleman [63] and Zavattieri and Espinosa [64]), time dependent fracture processes (Tijssens [52], Allen and Searcy [65]), and also near-threshold fatigue behaviour (Deshpande et al. [66]).

Thus, the cohesive model has been proved to be effective in the description of several problems and with different materials. One of the key issues in the application of this model is the choice of the material law within the cohesive zone. It is in fact clear that the traction-separation law is not known *a priori* and may change strongly for different materials. In the above cited papers, cohesive laws have been used with different traction-separation formulations. Several investigations focus on the effect of the shape of the traction-separation function on the resulting fracture behaviour [48, 53, 55, 56]. Tvergaard and Hutchinson [56, 57] came to the conclusion that this effect can be relatively weak.

Eventually, in the last few years, in order to explain the size effects upon the parameters of the cohesive crack model, Carpinteri [10, 11] applied fractal geometry concepts and described the influence of the microstructural disorder typical for most of quasi-brittle materials. The fractal approach was further developed by Carpinteri et al. [14, 67]. Recently, an improvement of the cohesive crack model, the so-called (scale-invariant) *fractal cohesive crack model* (Carpinteri et al. [68]), has been proposed and applied to interpret the most extensive experimental tensile data from concrete specimens tested over a broad range of scales (Carpinteri and Ferro [12], van Mier and van Vliet [69]). This topic will be extensively recalled in the present work, see Section 3.1.2.

### 2.2.1 Cohesive interpretation of the beam model

The linear elastic behaviour of a three point bending initially uncracked beam may be represented by the following dimensionless equation:

$$\tilde{P} = \frac{4}{\lambda^3} \tilde{\delta} \quad (25)$$

where the dimensionless load and central deflection are respectively given by:

$$\tilde{P} = \frac{Pl}{\sigma_u t h^2} \quad (26)$$

$$\tilde{\delta} = \frac{\delta l}{\varepsilon_u h^2} \quad (27)$$

with  $l$  = beam span,  $h$  = beam depth,  $t$  = beam thickness.

Once the ultimate tensile strength  $\sigma_u$  is achieved at the lower beam edge, a fracturing process in the central cross-section is supposed to start. Such a process admits a limit-situation like that in Fig. 5. The limit stage of the fracturing and deformation process may be considered as that of two rigid parts connected by the hinge A in the

upper beam edge. The equilibrium of each part is ensured by the external load, the support reaction and the closing cohesive forces. The latter depend on the distance between the two interacting surfaces: increasing the distance  $w$ , the cohesive forces decrease till they vanish for  $w \geq w_c$ .

The geometrical similitude of the triangles ABC and AB'C' in Fig.5 provides:

$$\frac{\delta}{l/2} = \frac{w_c/2}{x} \quad (28)$$

where  $x$  is the extension of the triangular distribution of cohesive forces. Eq. (28) can be rearranged as:

$$x = \frac{w_c l}{4\delta} \quad (29)$$

The rotational equilibrium round point A is possible for each beam part only if the moments of support reaction and cohesive forces respectively are equal:

$$\frac{P l}{2} = \frac{\sigma_u x t x}{2} \quad (30)$$

Recalling Eq. (29), the relation between load and deflection may be obtained:

$$P = \frac{\sigma_u t}{24} \frac{1}{\delta^2} \quad (31)$$

Eq. (31) can be put into dimensionless form:

$$\tilde{P} = \frac{1}{6} \left( \frac{s_E \lambda^2}{\varepsilon_u \delta} \right) \quad (32)$$

While the linear Eq. (25) describes the elastic behaviour of the beam initially uncracked, the hyperbolic Eq. (32) represents the asymptotical behaviour of the same beam, totally cracked. Eq. (25) is valid only for load values lower than that producing the ultimate tensile strength at the lower beam edge:

$$\tilde{P} \leq \frac{2}{3} \quad (33)$$

On the other hand, Eq. (32) is valid only for deflection values higher than that producing a cohesive zone of extension  $x$  equal to the beam depth  $b$ :

$$x \leq h \quad (34)$$

From Eqs. (29) and (34) it follows:

$$\tilde{\delta} \geq \frac{s_E \lambda^2}{2\varepsilon_u} \quad (35)$$

The bounds (33) and (35), upper for load and lower for deflection respectively, can be transformed into two equivalent bounds, both upper for deflection and load. Eqs. (25) and (33) provide:

$$\tilde{\delta} \leq \frac{\lambda^3}{6} \quad (36)$$

whereas Eqs. (32) and (35):

$$\tilde{P} \leq \frac{2}{3} \quad (37)$$

Conditions (33) and (37) are identical. Therefore, a stability criterion for elastic-softening beams may be obtained comparing Eqs. (35) and (36). When the two domains are separated, it is presumable that the two  $P$ - $\delta$  branches - linear and hyperbolic - are connected by a regular curve (Fig. 6a). On the other hand, when the two domains are partially overlapped, it is well-founded to suppose them as connected by a curve with highly negative or even positive slope (Fig. 6b).

Unstable behaviour and catastrophic events (snap-back) may be possible for:

$$\frac{s_E \lambda^2}{2\varepsilon_u} \leq \frac{\lambda^3}{6} \quad (38)$$

and the brittleness condition for the three point bending geometry becomes:

$$\frac{s_E}{\varepsilon_u \lambda} \leq \frac{1}{3} \quad (39)$$

Even in this case, the system is brittle for low brittleness numbers  $s_E$ , high ultimate strains and large slendernesses  $\lambda$ .

It is therefore evident that the relative brittleness for a structure is dependent on loading condition and external constraints, in addition to material properties, size-scale and slenderness. For instance, uniaxial tension is more unstable than three point bending:  $B \leq 1/2$  (Carpinteri [70]), whilst in bending  $B \leq 1/3$ .

As previously discussed, the global brittleness of the beam can be defined as the ratio of the ultimate elastic energy contained in the body to the energy dissipated by fracture:

$$\text{Brittleness} = \frac{\frac{1}{2} P_u \delta_u}{\mathcal{G}_F S} = \frac{\frac{1}{18} \sigma_u \varepsilon_u h t l}{\mathcal{G}_F h t} = \frac{1}{18B} \quad (40)$$

Such a ratio is higher than unity when:

$$\frac{s_E}{\varepsilon_u \lambda} \leq \frac{1}{18} \quad (41)$$

Eq. (41) represents a stricter condition for global structural brittleness compared with Eq. (39).

## 2.3 Mode I problems

The analyses discussed in this section concern the behaviour of concrete elements in Mode I conditions (Three Point Bending Test - TPBT). For reasons of symmetry, the crack trajectory is known a priori. The numerical results, based on the cohesive model, were obtained using the Finite Element Code FR.ANA. (FRacture ANALysis Carpinteri [4, 21, 23], Carpinteri et al. [37], Carpinteri [42], Carpinteri et al. [43, 44]).

An extensive series of analyses was carried out from 1984 to 1989 by A. Carpinteri and co-workers, and some

of the results obtained are mentioned later [4, 21, 23, 37, 42-44]. The experimental results can be found in Colombo and Limido [71], Bocca et al. [72] and in the RILEM report [73]. The cases described in the reference papers regard three  $\ell/h$  ratios (4, 8 and 16), and four  $a_0/h$  ratios (0.00, 0.10, 0.30, 0.50), see, for instance, Figs. 10 and 14. For each ratio, the response was analyzed for different values of the brittleness number,  $s_E$ , ranging from  $2 \times 10^{-2}$  to  $2 \times 10^{-5}$ .

As can be seen from the diagrams, the brittleness number  $s_E$  has a decisive effect on the structural response of the element: by increasing  $s_E$ , the behaviour of the element changes from brittle to ductile, as already stated. Hence, the structural response is not described by the parameters  $\sigma_u$ ,  $\mathcal{G}_F$  and  $h$  independently, but rather by a combination of these parameters, as expressed by the brittleness number  $s_E$ .

A comparison between the results obtained with the Finite Element Method and those provided by the Boundary Element Method can be found in Cen and Maier [46] and Maier et al. [74]. The agreement between the results is excellent: both implementations of the cohesive model are able to describe snap-back phenomena.

### 2.3.1 Numerical implementation

If a three point bending slab of elastic-softening material is considered, the displacement discontinuities on the center line may be expressed as follows:

$$w(x) = \int_0^h K(x, y) \sigma(y) dy + C(x)P + \Gamma(x) \quad (42)$$

for  $0 \leq x < h$

where  $K$  and  $C$  are the influence functions of cohesive forces and external load respectively, and  $\Gamma$  are the crack openings due to the specimen weight. If a stress-free crack of length  $a$  has developed with a cohesive zone of length  $\Delta a$ , the following additional conditions are to be taken into account:

$$\sigma(y) = 0 \quad \text{for } 0 \leq y \leq a \quad (43a)$$

$$\sigma(y) = \sigma_u \left( 1 - \frac{w(y)}{w_c} \right) \quad \text{for } a \leq y \leq a + \Delta a \quad (43b)$$

$$w(x) = 0 \quad \text{for } a + \Delta a \leq x \leq h \quad (43c)$$

Eqs. 42 and 43 can be rearranged as follows:

$$w(x) = \int_a^{a+\Delta a} K(x, y) \left( 1 - \frac{w(y)}{w_c} \right) \sigma_u dy + \int_{a+\Delta a}^h K(x, y) \sigma(y) dy + C(x)P + \Gamma(x) \quad (44a)$$

$$\text{for } 0 \leq x \leq (a + \Delta a) \quad (44b)$$

$$w(x) = 0 \quad (44c)$$

$$\text{for } (a + \Delta a) \leq x < h \quad (44d)$$

The function  $\sigma(y)$  depends on the distribution  $w(x)$  and on the external load  $P$ . Therefore, for each value of  $P$ , Eq. (44b) represents an integral equation for the unknown function  $w$ . On the other hand, the beam deflection is given by:

$$\delta = \int_0^h C(y)\sigma(y)dy + D_P P + D_\gamma \quad (45)$$

where  $D_P$  is the deflection for  $P = 1$  and  $D_\gamma$  is the deflection due to the specimen weight.

A numerical procedure is implemented to simulate a loading process where the parameter incremented step by step is the fictitious crack depth. Real (or stress-free) crack depth, external load and deflection are obtained at each step after an iterative computation. The closing stresses acting on the crack surfaces are replaced by nodal forces (Fig. 7). The intensity of these forces depends on the opening of the fictitious crack,  $w$ , according to the  $\sigma - w$  constitutive law of the material (Fig. 4). When the tensile strength  $\sigma_u$  is achieved at the fictitious crack tip (Fig. 7), the top node is opened and a cohesive force starts acting across the crack, while the fictitious crack tip moves to the next node.

With reference to the three point bending test (TPBT) geometry in Fig. 8, the nodes are distributed along the potential fracture line. The coefficients of influence in terms of node openings and deflection are computed by a finite element analysis where the fictitious structure in Fig. 8 is subjected to  $(n+1)$  different loading conditions.

Consider the TPBT in Fig. 9 with the initial crack tip in the node  $k$ . The crack opening displacements at the  $n$  fracture nodes may be expressed as follows:

$$\{w\} = [K]\{F\} + \{C\}P + \{\Gamma\} \quad (46)$$

being:

- $\{w\}$  the vector of the crack opening displacements,
- $[K]$  the matrix of the coefficients of influence (nodal forces),
- $\{F\}$  the vector of the nodal forces,
- $\{C\}$  the vector of the coefficients of influence (external load),
- $P$  the external load,
- $\{\Gamma\}$  the vector of the crack opening displacements due to the specimen weight.

On the other hand, the initial crack is stress-free and therefore:

$$F_i = 0 \quad \text{for } i = 1, 2, \dots, (k-1) \quad (47a)$$

while at the ligament there is no displacement discontinuity:

$$w_i = 0 \quad \text{for } i = k, (k+1), \dots, n \quad (47b)$$

Eqs. (46) and (47) constitute a linear algebraical system of  $2n$  equations and  $2n$  unknowns, i.e., the elements of vectors  $\{w\}$  and  $\{F\}$ . If load  $P$  and vector  $\{F\}$  are known, it is possible to compute the beam deflection,  $\delta$ :

$$\delta = \{C\}^T \{F\} + D_P P + D_\gamma \quad (48)$$

After the first step, a cohesive zone forms in front of the real crack tip (Fig. 9), say between nodes  $j$  and  $l$ . Then Eqs. (47) are replaced by:

$$F_i = 0 \quad \text{for } i = 1, 2, \dots, (j-1) \quad (49a)$$

$$F_i = F_u \left(1 - \frac{w_i}{w_c}\right) \quad \text{for } i = j, (j+1), \dots, l \quad (49b)$$

$$w_i = 0 \quad \text{for } i = l, (l+1), \dots, n \quad (49c)$$

where  $F_u$  is the ultimate strength nodal force (Fig. 7):

$$F_u = h \frac{\sigma_u}{m} \quad (50)$$

Eqs. (46) and (49) constitute a linear algebraical system of  $(2n+1)$  equations and  $(2n+1)$  unknowns, i.e., the elements of vectors  $\{w\}$  and  $\{F\}$  and the external load  $P$ .

At the first step, the cohesive zone is missing ( $l = j = k$ ) and the load  $P$  producing the ultimate strength nodal force at the initial crack tip (node  $k$ ) is computed. Such a value  $P_1$ , together with the related deflection  $\delta_1$  computed through Eq. (48) gives the first point of the  $P - \delta$  curve.

At the second step, the cohesive zone is between the nodes  $k$  and  $(k+1)$ , and the load  $P_2$  producing the force  $F_u$  at the second fictitious crack tip (node  $k+1$ ) is computed. Eq. (48) then provides the deflection  $\delta_2$ . At the third step, the fictitious crack tip is in the node  $(k+2)$ , and so on. The present numerical program simulates a loading process where the 0 parameter is the fictitious crack depth.

On the other hand, real (or stress-free) crack depth, external load and deflection are obtained at each step after an iterative procedure.

The program stops with the untieing of the node  $n$  and, consequently, with the determination of the last couple of values  $F_n$  and  $\delta_n$ . In this way, the complete load-deflection curve is automatically plotted by the computer.

### 2.3.2 Numerical simulations

#### Strain localization and apparent strength of initially uncracked slabs

Some dimensionless load-deflection diagrams for a concrete-like material are plotted in Fig. 10, with  $a_0/h = 0.0$ ,  $\varepsilon_u = 0.87 \cdot 10^{-4}$ ,  $\nu = 0.1$ ,  $t = h$ ,  $l = 4h$ , and by varying the non-dimensional number  $s_E$ .

The specimen behaviour is brittle (snap-back) for low  $s_E$  numbers, i.e., for low fracture toughnesses  $\mathcal{G}_F$ , high tensile strengths,  $\sigma_u$ , and/or large sizes,  $h$ . For  $s_E \lesssim 10.45 \cdot 10^{-5}$ , the  $P - \delta$  curve presents positive slope in the softening branch and a catastrophic event occurs if the loading process is deflection-controlled. Such indenting branch is not virtual only if the loading process is controlled by a monotonically increasing function of time (Fairhurst et al. [75], Rokugo et al. [76]) like, for example, the displacement discontinuity across the crack (Biolzi et al. [77]). On the other hand, Eq. (39) gives:  $s_E \leq 11.60 \cdot 10^{-5}$ . Such a condition reproduces that shown in Fig. 10 very accurately, whereas Eq. (41) appears too severe. When the post-peak behaviour is kept under control up to the complete structure separation, the area delimited by load-deflection curve and deflection-axis represents the product of fracture energy,  $\mathcal{G}_F$ , and initial cross-section area,  $ht$ .

The maximum loading capacity  $P_{Cohes}$  of initially uncracked specimens with  $l = 4h$  is obtained from Fig. 10. On the other hand, the maximum load of ultimate strength is given by:

$$P_{U.S.} = \frac{2}{3} \frac{\sigma_u t h^2}{l} \quad (51)$$

The values of the ratio  $P_{Cohes}/P_{U.S.}$  may also be regarded as the ratio of the apparent tensile strength  $\sigma_f$  (given by the maximum load  $P_{Cohes}$  and applying Eq. (51)) to the true tensile strength  $\sigma_u$  (considered material constant). It is evident from Fig. 11 that the results of the cohesive crack model tend to those of the ultimate strength analysis for low  $s_E$  values:

$$\lim_{s_E \rightarrow 0} P_{Cohes} = P_{U.S.} \quad (52)$$

Therefore, only for comparatively large specimen sizes the tensile strength  $\sigma_u$  can be obtained as  $\sigma_u = \sigma_f$ . With the usual laboratory specimens, always an apparent strength higher than the true one is found.

As a limit case, for the size  $h \rightarrow 0$  or fracture energy  $\mathcal{G}_F \rightarrow \infty$  (elastic-plastic material in tension), i.e., for  $s_E \rightarrow \infty$ , the apparent strength  $\sigma_f \rightarrow 3\sigma_u$ . In fact, in the centre of the beam, the uniform stress distribution (Fig. 12) produces a plastic hinge with a resistant moment which is twice the classical moment of the bi-rectangular limit stress distribution (elastic-perfectly plastic material in tension and compression).

The fictitious crack depth at the maximum load is plotted as a function of  $1/s_E$  in Fig. 13. The brittleness increase for  $s_E \rightarrow 0$  is evident also from this diagram, the process zone at  $dP/d\delta = 0$  tending to disappear (brittle collapse), whereas it tends to cover the whole ligament for  $s_E \rightarrow \infty$  (ductile collapse). On the other hand, the real (or stress-free) crack depth at the maximum load is always zero for each value of  $s_E$ . This means that the slow crack growth does not start before the softening stage. Therefore, neither the slow crack growth occurs nor the cohesive zone develops before the peak, when  $s_E \rightarrow 0$ .

Recalling once again Figs. 11 and 13, it is possible to state that, the smaller the brittleness number  $s_E$  is, the more accurate the snap-back is in reproducing the perfectly-brittle ultimate strength instability ( $a_0/h = 0$ ).

### Cohesive crack propagation and fictitious fracture toughness of initially cracked slabs

The mechanical behaviour of three point bending slabs with initial cracks is investigated on the basis of the same cohesive numerical model presented in the preceding section. Some dimensionless load-deflection diagrams are represented in Fig. 14, for  $a_0/h = 0.5$ ,  $\varepsilon_u = 0.87 \cdot 10^{-4}$ ,  $\nu = 0.1$ ,  $t = h$ ,  $l = 4h$ , and by varying the brittleness number  $s_E$ . The initial crack makes the specimen behaviour more ductile than in the case of initially uncracked specimen. For the set of  $s_E$  numbers considered in Fig. 14, the snap-back does not occur.

The area delimited by load-deflection curve and the deflection axis represents the product of fracture energy,  $\mathcal{G}_F$ , and initial ligament area,  $(h - a_0)t$ . The areas under the  $P - \delta$  curves are thus proportional to the respective  $s_E$  numbers, in Fig. 10 as well as in Fig. 14. This simple result is due to the assumption that energy dissipation occurs only on the fracture surface, whereas in reality energy is also dissipated in a damage volume around the crack tip, as assumed by Carpinteri and Sih [78] and proved by Cedolin et al. [79].

The maximum loading capacity  $P_{Cohes}$  according to the cohesive crack model, is obtained from Fig. 14. On the other hand, the maximum load  $P_{L.E.F.M.}$  of brittle fracture can be obtained from the Linear Elastic Fracture Mechanics relation, Eq. (10), with  $K_{IC} = [\mathcal{G}_F E]^{1/2}$  (plane stress condition).

The values of the ratio  $P_{Cohes}/P_{L.E.F.M.}$  are reported as functions of the inverse of the brittleness number in Fig. 15. Such a ratio may also be regarded as the ratio of the fictitious fracture toughness (given by the maximum load  $P_{Cohes}$ ) to the true fracture toughness (considered as a material constant).

It is evident that, for low  $s_E$  numbers, the results of the Cohesive crack model tend to those of Linear Elastic Fracture Mechanics:

$$\lim_{s_E \rightarrow 0} P_{Cohes} = P_{L.E.F.M.} \quad (53)$$

and therefore, the maximum loading capacity can be predicted applying the simple condition  $K_I = K_{IC}$ . It appears that the true fracture toughness  $K_{IC}$  of the material can be obtained only with very large specimens. In fact, with the laboratory specimens, a fictitious fracture toughness lower than the true one is always measured, as in Carpinteri [19, 21, 26], Barr and Bear [80], Ingraffea and Saouma [81], Kasperkiewicz et al. [82], Li and Liang [83], Li et al. [84], Shah [85], Walsh [86], Zaitsev and Kovler [87], Ziegeldorf et al. [88], Carpinteri and Valente [89].

### 3 The fractal model

Before entering the details of fractal fracture mechanics applied to heterogeneous and disordered materials, a brief review of the applications of fractal geometry concepts to material science is addressed. Nevertheless, the following list of references is not at all complete, since this research field is nowadays very spread inside the scientific community.

It was Mandelbrot himself who applied the new concept from his book [90] to the fracture profiles of metals [91]. After this paper, the attempts to apply fractals to fracture have grown exponentially. To quote some of the first papers devoted to characterize fractal damage and fracture in metals, we can cite the papers by Kleiser & Bocek [92] about slip lines and by Dauskart, Haubensak and Ritchie [93] about fracture surfaces.

Inside this field, we can distinguish three different aspects: the first one deals with the methods to compute the fractal dimension of the fracture surfaces, the second one is devoted to the analysis of the correlation between fractal features and microstructural properties whereas the third aspect tries to highlight the consequences of fractality onto the mechanical behavior of materials.

For what concerns the first aspect, the reader is referred to the paper by Charkaluc [94] where the different methods are analyzed critically and compared: the compass method, the Minkowski method, the box counting method, the variation method, the slit island method. Theoretically, all the methods yield the same values of the fractal dimension. On the other hand, the result can change when applied to specific cases: it is therefore of the maximum importance to find the suitable method before trying to find a correlation between fractal fracture properties and mechanical features.

About the second aspect, i.e. the link between microstructure and fractal sets, we can cite, among the others, the papers by Carpinteri et al. [95, 96] for what concerns aggregative materials and the paper by Panin et al. [97] about metal mesostructure.

The third aspect is the most theoretical one. It tries to answer the question: "What are the mechanical consequences of the presence of a fractal crack?". Answering the former question will be the subject of the following section. Particularly, it will be shown that the first consequence is the presence of size effects. Beyond the efforts of the present authors (begun with the paper [10]), and the pioneering work by Mosolov [98], we have to cite the work done by Borodich [99], showing how microcracks can give rise to fractal patterns, the paper by Balankin [100] dealing with self affine cracks and the strong theoretical contribution by Panagiotopoulos [101]. More recently, a further development has been provided by Yavari et al. [102], who pointed out how, in the presence of a fractal crack, the basic modes of fracture are six instead of the usual three.

Finally, from an experimental point of view, it is worth noting that the fracture surfaces usually cannot be de-

scribed by simple self-similar fractal sets. In general a better description can be achieved by means of self-affine fractal sets [100] or by a multifractal analysis [103]. Focusing the attention only to concrete-like materials, the literature is nevertheless rather large: here we can cite [9, 104] among the first papers and [105] among the most recent ones.

In what follows, we will analyze the effect of fractal patterns in the failure mechanism of materials with a heterogeneous microstructure, i.e. the fractal features are assumed *a priori*. Since the structural behavior of this kind of materials is usually described by the cohesive crack model, we will show how this model can be updated in order to take into account the rising of fractal patterns, giving birth to the so-called *fractal cohesive crack model* [68].

#### 3.1 The effect of the microstructural disorder

Dealing with direct tension tests of unnotched specimens, it is clear that, according to the cohesive crack model presented in the previous Section, no size effect should rise. Nevertheless, their presence received several experimental confirmations.

The explanation of the size effects upon tensile fracture properties of concrete specimens, especially in direct tension tests, is an ongoing matter of discussion inside the scientific community. A sound approach to this problem has been proposed by Carpinteri since 1994 by means of *fractal geometry*. Carpinteri [10, 11] applied fractal geometry concepts to describe the influence of the microstructural disorder typical of most of quasi-brittle materials. The basic concepts of the fractal approach were further developed by Carpinteri et al. [14, 67]. Recently, an improvement of the cohesive crack model, the (scale-invariant) fractal cohesive crack model (Carpinteri et al. [68]), was proposed and applied to the most important tensile experimental data from concrete specimens tested in a broad range of scales (Carpinteri and Ferro [12], van Mier and van Vliet [69]).

##### 3.1.1 The fractal approach

The fundamental reason of size effect rising in quasi-brittle material structures is damage localization. In the previous sections we showed how the cohesive crack model is able to catch this peculiar behaviour in the bending configuration. For other configurations, the reader is referred to the review paper of Carpinteri et al. [106]. More in detail, the cohesive crack model is able to simulate those tests where high stress gradients are present, i.e. tests on pre-notched specimens. In these cases, the cohesive crack model captures the ductile-to-brittle transition occurring by increasing the size of the structure. On the other hand, smaller but nevertheless relevant size effects are encountered in uniaxial tension tests on dog-bone shaped specimens, where much smaller stress gra-

dients are present. In this case, size effects should be inherent to the material behavior rather than to the stress-intensification.

Apart from the tests carried out by Bažant and Pfeiffer [107] in a limited scale range (1:4), uniaxial tensile tests on dog-bone shaped specimens were performed by Carpinteri and Ferro [12], with controlled boundary conditions, in a scale range 1:16, and by van Mier and van Vliet [69], with rotating boundary conditions, in a scale range 1:32. The tests, in both cases, proved that the physical parameters characterizing the cohesive law are scale-dependent, thus showing the limits of Hillerborg's model. By increasing the size of the specimen, the peak of the cohesive law decreases while the tail rises. In other words, the tensile strength decreases while the fracture energy as well as the critical displacement increase.

A consistent explanation of the size effects affecting the cohesive law parameters in direct tension test was provided by Carpinteri [10, 11] and by Carpinteri et al. [68] assuming *fractal* damage domains. This hypothesis is motivated by the disorder characterizing the microstructure of most of quasi-brittle materials in a broad range of scales. Size effects in tests without high stress gradients can therefore be seen as a consequence of the heterogeneous microstructure of concrete and rocks. Since the flaw distribution in quasi-brittle materials is often self-similar (i.e. it looks the same at different magnification levels), the microstructure can be correctly modelled by fractal sets.

Fractal sets are characterized by non-integer dimensions (Feder [5]). For instance, the dimension  $\alpha$  of a fractal set in the plane can vary between 0 and 2. Accordingly, increasing the measure resolution, its length tends to zero if its dimension is smaller than 1 or tends to infinity if it is larger. In these cases, the length is a nominal, useless quantity, since it diverges or vanishes as the measure resolution increases. A finite measure can be achieved only using non-integer quantities, such as meters raised to  $\alpha$ .

Analogously, if the stress and strain localization occurs in a fractal damaged zone, the nominal quantities (ultimate strength, critical strain, fracture energy) depend on the resolution used to measure the set where stress, strain and energy dissipation take place. In the limit of a very high measure resolution, the stress and the strain should be infinite, while the dissipated energy should be zero. Finite values can be obtained only introducing fractal quantities, i.e. mechanical quantities having non-integer physical dimensions. On the other hand, if the measure resolution is fixed, the nominal quantities undergo size effects. More specifically, the fractal strain localization explains the observed increasing tail of the cohesive law as the specimen size increases (see van Mier and van Vliet [108]), i.e., it clarifies the scaling of the critical displacement  $w_c$ . Similarly, the fractal stress localization explains the experimentally observed decreasing peak of the cohesive law while increasing the specimen size, i.e., it clarifies the scaling of the tensile strength  $\sigma_u$ . Finally, the scaling

of the fracture energy is a consequence of the invasive fractality of the set where energy dissipates (i.e. the fracture surface or a damaged band). According to the fractal approach, the scaling of the cohesive law parameters are represented by power laws whose exponents are linked by a relation.

Without entering the details, we want to stress that the hypothesis of the fractal damage domain in quasi-brittle material failure is not a mathematical abstraction, since fractal patterns have been detected in several experiments (see, for instance, Carpinteri et al. [109, 110]). Furthermore, for what concerns the concrete case, another explanation of the fractal features of the damaged zones has been recently derived from the analysis of the aggregate size distribution (Carpinteri et al. [95], Carpinteri and Cornetti [111]). This *stereological* analysis confirmed the range of the values of the strength and fracture energy power law exponents previously conjectured by Carpinteri upon dimensional analysis arguments [11].

The analyses of the fracture surfaces have shown that the fractal behavior is more evident at the smaller scales. At the larger scales, the disorder and its influence onto the mechanical properties seem to diminish. While classical (i.e. self-similar) fractal sets cannot catch this trend, the self-affine fractals can. The scaling laws previously derived have been therefore extended to the self-affine case, leading to the definition of the *multifractal scaling laws* (Carpinteri and Chiaia [112, 113]) for the strength (Carpinteri et al. [67, 114]), for the fracture energy (Carpinteri and Chiaia [14, 115]), and, more recently, for the critical displacement (Carpinteri et al. [95]). In this research field, these concepts have been applied not only to tensile tests, but also to explain the R-curve material behavior (Carpinteri and Chiaia [116]) and to interpret the results of bending (Carpinteri et al. [117]) and compression (Carpinteri et al. [118]) tests. Finally, Konstantinidis et al. [119], Efraimidis et al. [120] compared the size effect prediction provided by the fractal approach with the one given by the gradient theory approach.

Another important research direction has been recently opened by Carpinteri and Cornetti [121]. They have tried to generalize the classical differential equations of the continuum mechanics to fractal media. Since fractal functions, because of their irregularity, cannot be solution of any differential equations, they argued that suitable mathematical operators should replace the integro-differential operators of the classical calculus (Carpinteri and Mainardi [122]). The attention was drawn to the local fractional calculus operators recently introduced by Kolwankar [123] stemming from fractional calculus. Fractional calculus is the branch of the calculus dealing with integrals and derivative of any order. The interested reader is referred to the following specific papers: Carpinteri et al. [124, 125, 126]. Here we just want to point out that the order of differentiation is linked to the fractal dimension of the domain where the differential equations hold and that, by local fractional calculus, the authors succeeded in proving the Principle of Virtual Work for

fractal media.

We saw that the cohesive model parameters are size-dependent. In order to get true material parameters, we are forced to introduce quantities with anomalous (non-integer) physical dimensions: the fractal tensile strength, the fractal critical strain and the fractal fracture energy. Thanks to their non-integer physical dimensions, they intrinsically include the fractal dimensions of the sets where stress, strain and energy dissipation localize.

In the next section, we will focus our attention upon these fractal mechanical quantities, in terms of which it is possible to define a scale-invariant cohesive law, which represents a true material property. Together with the linear elastic constitutive law valid for the undamaged part of the material, these two laws define a material model that we call the (size-independent) *fractal cohesive crack model*. The model will be applied to the results of the tests carried out by Carpinteri and Ferro [127] and by van Mier and van Vliet [69], in order to prove the soundness of the fractal approach to the size effect prediction.

### 3.1.2 Scale-independent cohesive crack model

In order to introduce the fractal cohesive crack model, we have to consider separately the size effects upon the three parameters characterizing the cohesive law.

Let us start analyzing the size effect upon the tensile strength considering a concrete specimen subjected to tension (Fig. 16a). Recent experimental results about porous concrete microstructure (Carpinteri et al. [110]) as well as a stereological analysis of concrete flaws (Carpinteri and Cornetti [111]) led us to believe that a consistent modelling of damage in concrete can be achieved by assuming that the rarefied resisting sections in correspondence of the critical load can be represented by stochastic lacunar fractal sets with dimension  $2 - d_\sigma$  ( $d_\sigma \geq 0$ ). From fractal geometry, we know that the area of lacunar sets is scale-dependent and tends to zero as the resolution increases: the tensile strength should be infinite, which is meaningless. Finite measures can be obtained only with non-integer (fractal) dimensions. For the sake of simplicity, let us represent the specimen resistant cross-section as a Sierpinski carpet built on the square of side  $b$  (fig. 16b). The fractal dimension of this lacunar domain is 1.893 ( $d_\sigma = 0.107$ ). The assumption of Euclidean domain characterizing the classical continuum theory states that the maximum load  $F$  is given by the product of the strength  $\sigma_u$  times the nominal area  $A_0 = b^2$ , whereas, in our model,  $F$  equals the product of the (Hausdorff) fractal measure (Feder [5])  $A_{res}^* \sim b^{2-d_\sigma}$  of the Sierpinski carpet times the *fractal tensile strength*  $\sigma_u^*$  (Carpinteri [10]):

$$F = \sigma_u A_0 = \sigma_u^* A_{res}^* \quad (54)$$

where  $\sigma_u^*$  presents the anomalous physical dimensions  $[F][L]^{-(2-d_\sigma)}$ . The fractal tensile strength is the true material constant, i.e., it is scale-invariant. From Eq. (54)

we obtain the scaling law for tensile strength:

$$\sigma_u = \sigma_u^* b^{-d_\sigma} \quad (55)$$

i.e. a power law with negative exponent  $-d_\sigma$ . Eq. (55) represents the negative size effect on tensile strength, experimentally revealed by several authors. Experimental and theoretical results allow us to affirm that  $d_\sigma$  can vary between the lower limit 0 - canonical dimensions for  $\sigma_u^*$  and absence of size effect on tensile strength - and the upper limit  $1/2 - \sigma_u^*$  with the dimensions of a stress-intensity factor and maximum size effect on tensile strength (as in the case of LEFM).

Secondly, let us consider the work  $W$  necessary to break a concrete specimen of cross section  $b^2$  (Fig. 16a). It is equal to the product of the fracture energy  $\mathcal{G}_F$  times the nominal fracture area  $A_0 = b^2$ . On the other hand, the surface where energy is dissipated is not the flat cross-section: it is the crack surface, whose area  $A_{dis}$  diverges as the measure resolution tends to infinity because of its roughness at every scale. Therefore the fracture energy should be zero, which is meaningless. Finite values of the measure of the set where energy is dissipated can be achieved only via non-integer fractal dimension. For the sake of simplicity, let us represent the crack surface as a Von Kock surface built on the square of side  $b$  (Fig. 16c). The fractal dimension of this invasive domain is 2.262, i.e.  $2 + d_G$  ( $d_G = 0.262$ ). The classical cohesive crack model states that the failure work  $W$  is given by the product of the fracture energy  $\mathcal{G}_F$  times the nominal area  $A_0 = b^2$ , whereas, in our model,  $W$  equals the product of the fractal (Hausdorff) measure  $A_{dis}^* \sim b^{2+d_G}$  of the Von Kock surface times the *fractal fracture energy*  $\mathcal{G}_F^*$  (Carpinteri [10]):

$$W = \mathcal{G}_F A_0 = \mathcal{G}_F^* A_{dis}^* \quad (56)$$

$$\mathcal{G}_F = \mathcal{G}_F^* b^{d_G} \quad (57)$$

$\mathcal{G}_F^*$  is the true scale invariant material parameter, whereas the nominal value  $\mathcal{G}_F$  is subjected to a scale effect described by a positive power law.

Now we turn our attention to the deformation inside the zone where damage localizes (the so-called damaged band). We assume that the strain field presents fractal patterns. This could appear strange at a first glance; on the contrary, fractal strain distributions are rather common in material science. For instance, in some metals, the so-called slip-lines develop with typical fractal patterns (Kleiser and Bocek [92]). Fractal crack networks develop also in dry clay or in old paintings under tensile stresses due to shrinkage. Thus, as representative of the damaged band, consider now the simplest structure, a bar subjected to tension (Fig. 17a), where, at the maximum load, dilation strain tends to concentrate into different softening regions, while the rest of the body undergoes elastic unloading.

Assume, for instance, that the strain is localized at cross-sections whose projections onto the longitudinal

axis are provided by the triadic Cantor set, whose dimension is  $\ln 2 / \ln 3 = 0.639$ ; the displacement function at rupture can be represented by a Cantor staircase graph, sometimes also called devil's staircase (Fig. 17a). The strain defined in the classical manner is meaningless in the singular points, as it diverges. This drawback can be overcome by introducing a fractal strain. Let us indicate with  $1 - d_\varepsilon$  ( $d_\varepsilon \geq 0$ ) the fractal dimension of the lacunar projection of the damaged sections (in this case  $d_\varepsilon = 0.361$ ). According to the fractal measure of the damage line projection, the total elongation  $w_c$  of the band at rupture must be given by the product of the Hausdorff measure  $b^* \sim b^{(1-d_\varepsilon)}$  of the Cantor set times the *critical fractal strain*  $\varepsilon_c^*$ , while in the classical continuum theory it equals the product of the length  $b$  times the critical strain  $\varepsilon_c$ :

$$w_c = \varepsilon_c b = \varepsilon_c^* b^{(1-d_\varepsilon)} \quad (58)$$

$$\varepsilon_c = \varepsilon_c^* b^{-d_\varepsilon} \quad (59)$$

where  $\varepsilon_c^*$  has the anomalous physical dimension  $[L]^{d_\varepsilon}$ . The fractal critical strain is the true material constant, i.e. it is the only scale-invariant parameter governing the kinematics of the damaged band. On the other hand, Eq. (58) states that the scaling of the critical displacement is described by a power law with positive exponent  $(1 - d_\varepsilon)$ . The fractional exponent  $d_\varepsilon$  is intimately related to the degree of disorder in the mesoscopic damage process. When  $d_\varepsilon$  varies from 0 to 1, the kinematical control parameter  $\varepsilon_c^*$  moves from the canonical critical strain  $\varepsilon_c$  – of dimension  $[L]^0$  – to the critical crack opening displacement  $w_c$  – of dimension  $[L]^1$ . Therefore, when  $d_\varepsilon = 0$  (diffused damage, ductile behaviour), one obtains the classical response, i.e. collapse governed by the strain  $\varepsilon_c$ , independently of the bar length. In this case, continuum damage mechanics holds, and the critical displacement  $w_c$  is subjected to the maximum size effect ( $w_c \propto b$ ). On the other hand, when  $d_\varepsilon = 1$  (localization of damage onto isolated sections, brittle behaviour) fracture mechanics holds and the collapse is governed by the critical opening displacement  $w_c$ , which is size-independent as in the cohesive model.

The three size effect laws (55), (57), (58) of the cohesive law parameters are not completely independent one of the other. In fact, there is a relation among the scaling exponents that must be always satisfied. This means that, when two exponents are given, the third follows from the first two. In order to get this relation, suppose, for instance, to know  $d_\sigma$  and  $d_\varepsilon$ . Generalizing Eqs. (55) and (58) to the whole softening regime, we get  $\sigma = \sigma^* b^{-d_\sigma}$  and  $w = \varepsilon^* b^{(1-d_\varepsilon)}$ . These relationships can be considered as changes of variables and applied to the integral definition of the fracture energy:

$$\mathcal{G}_F = \int_0^{w_c} \sigma dw = b^{1-d_\varepsilon-d_\sigma} \int_0^{\varepsilon_c^*} \sigma^* d\varepsilon^* = \mathcal{G}_F^* b^{1-d_\varepsilon-d_\sigma} \quad (60)$$

Eq. (60) highlights the effect of the structural size on the fracture energy, as Eq. (57) does. Therefore, comparing

Eqs. (57) and (60), we get the relation among the exponents:

$$d_\sigma + d_\varepsilon + d_G = 1 \quad (61)$$

Note that, from a physical point of view, the geometrical relationship (61) states that, after the peak load, the energy is dissipated over the infinite lacunar sections where softening takes place inside the damaged band (Fig. 17b). This statement is not the same of considering the crack surface (Fig. 16c) as the region where dissipation takes place. It is nevertheless equivalent since it yields the same power law scaling (57), the fractal dimensions of the dissipation domains being larger than 2 in both cases.

While  $d_\varepsilon$  can get all the values inside the interval  $[0, 1]$ ,  $d_\sigma$  and  $d_G$  tend to be comprised between 0 and 1/2 (brownian disorder). Eq. (61) provides a strict restriction to the maximum degree of disorder, confirming that the sum of  $d_\sigma$  and  $d_G$  is always lower than 1, as previously asserted by Carpinteri [11] through dimensional analysis arguments.

It is interesting to note how, from Eq. (60), the fractal fracture energy  $\mathcal{G}_F^*$  can be obtained as the area below the fractal softening stress-strain diagram (Fig. 18b). During the softening regime, i.e. when dissipation occurs,  $\sigma^*$  decreases from the maximum value  $\sigma_u^*$  to 0, while  $\varepsilon^*$  grows from 0 to  $\varepsilon_c^*$ . In the meantime, the nondamaged parts of the bar undergo elastic unloading (Fig. 18a). We call the  $\sigma^*$ - $\varepsilon^*$  diagram the scale-independent or *fractal cohesive law*. Contrarily to the classical cohesive law, which is experimentally sensitive to the structural size, this curve should be an exclusive property of the material, it being able to capture the fractal nature of the damage process. The couple of constitutive laws  $\sigma$ - $\varepsilon$  and  $\sigma^*$ - $\varepsilon^*$  (Fig. 18) defines the *size-invariant (fractal) cohesive crack model*.

The model has been applied to the data obtained in 1994 by Carpinteri and Ferro [12, 127] for tensile tests on dog-bone shaped concrete specimens of various sizes under controlled boundary conditions (Fig. 19a). They interpreted the size effects on the tensile strength and the fracture energy by fractal geometry. Fitting the experimental results, they found the values  $d_\sigma = 0.14$  and  $d_G = 0.38$ . Some of the  $\sigma$ - $\varepsilon$  (stress vs. strain) and  $\sigma$ - $w$  diagrams are reported respectively in Fig. 19b and Fig. 19c, where  $w$  is the displacement localized in the damaged band, obtained by subtracting, from the total one, the displacement due to elastic and anelastic pre-peak deformation. Eq. (61) yields  $d_\varepsilon = 0.48$ , so that the fractal cohesive laws can be plotted in Fig. 19d. As expected, all the curves related to the single sizes tend to merge in a unique, scale-independent cohesive law. The overlapping of the cohesive laws for the different sizes proves the soundness of the fractal approach to the interpretation of concrete size effects.

More recently, van Mier and van Vliet [69] accurately performed tensile tests on dog-bone shaped concrete specimens over a wide scale range (1:32) under rotating boundary conditions (Fig. 21a). In Fig. 21b, the stress vs. strain diagrams are reported for different spec-

imen sizes: note the ductile-to-brittle transition represented by the steeper negative softening slope for the larger sizes. Moreover, Van Mier and Van Vliet plotted the cohesive law for specimens of different sizes and found that, increasing the specimen size, the peak of the curve decreases whereas the tail rises (van Mier and van Vliet [108]). In other words  $\sigma_u$  decreases whereas  $w_c$  and  $\mathcal{G}_F$  increases, thus confirming the prediction of the fractal model.

An analysis of the data obtained by van Mier and van Vliet [69] according to the fractal cohesive model is presented now. We considered the average values obtained for the different specimen sizes. The data of the smallest specimen size ( $D = 50$  mm) were not considered, since, as stated by the authors, secondary effects are present (e.g. the influence of the largest grains and the wall effect) that bias the results. Furthermore, the authors were not able to obtain the whole tail of the softening branch for the specimens of the larger sizes. In order to obtain the value of the fracture energy, they completed the cohesive laws via a linear extrapolation. This procedure, although rigorous, leads to an underestimate of the computed fracture energy since it does not respect the concavity of the curve. Therefore, we decided to complete the cohesive law diagrams in a somehow arbitrary way maintaining the concave shape for all the specimen sizes (Fig. 21c). Observing the interceptions of the curves with the axes, it is evident that the higher is the peak, the shorter is the tail.

Linear regressions in the bilogarithmic plots of tensile strength and fracture energy vs. specimen cross section size were performed (Fig. 20). We found respectively a fractal fracture energy  $\mathcal{G}_F^*$  equal to  $9.22 \times 10^{-2} \text{N mm}^{-1.09}$  and a fractal tensile strength  $\sigma_u^*$  equal to  $6.42 \text{N mm}^{-1.82}$ , with fractal exponents  $d_G = 0.09$  and  $d_\sigma = 0.18$ . The correlation coefficients were found to be respectively  $R_G = 0.995$  and  $R_\sigma = 0.990$ ; their values close to unity prove the soundness of the power law scaling. The relation (61) among the scaling exponents yields  $d_\varepsilon = 0.73$ , so that the fractal cohesive laws can be plotted in Fig. 21d. Once again the superposition of the different plots denotes the validity of the fractal cohesive model. Particularly, note the low scattering of the interceptions with the vertical and horizontal axes in respect to the ones of Fig. 21c: they represent respectively the fractal critical strain  $\varepsilon_c^*$  and the fractal tensile strength  $\sigma_u^*$ , while the area subtended by the fractal cohesive law diagrams provides  $\mathcal{G}_F^*$ . An even clearer representation is reported in Fig. 22, where different scales are used for low or high values of both the axes coordinates.

### 3.2 Local fractional calculus and fractal functions

Once the multiscale microstructure geometry has been described and the fractal mechanical quantities defined, we need suitable mathematical instruments to write differential equations in terms of such quantities and upon

such irregular domains.

As is well-known, fractals cannot be handled by classical calculus. No fractal function can be the solution of a classical differential equation. Therefore, it is argued that a new calculus should be developed which intrinsically includes a fractal structure (Carpinteri and Mainardi [122]). Recently Kolwankar [123], based on fractional calculus, defined new mathematical operators – the local fractional derivative and the fractal integral – that appear to be useful in the description of fractal processes. It is important to emphasize that, what seems to be really interesting in studying fractals via fractional calculus, are the non-integer physical dimensions that arise dealing with both fractional operators and fractal sets. This means to find the same scaling laws both from the analytic and geometric point of view.

Let us consider the classical fractional calculus. While classical calculus treats integrals and derivatives of integer order, fractional calculus is the branch of mathematics dealing with the generalization of integrals and derivatives to all real (and even complex) orders. There are various definitions of fractional differentio-integral operators, not necessarily equivalent to each other. A complete list of these definitions can be found in the fractional calculus treatises: Oldham and Spanier [128], Miller and Ross [129], Samko et al. [130], Podlubny [131]. These definitions have different origins. The most frequently used definition of a fractional integral of order  $q$  ( $q > 0$ ) is due to Riemann-Liouville and is a straightforward generalization to noninteger values of Cauchy formula for repeated integration:

$$\frac{d^{-q}f(x)}{[d(x-a)]^{-q}} = \frac{1}{\Gamma(q)} \int_a^x \frac{f(y)}{(x-y)^{1-q}} dy \quad (62)$$

From this formula, it appears logical to define the fractional derivative of order  $n-1 < q < n$  ( $n$  integer) as the  $n$ -th integer derivative of the  $(n-q)$ -th fractional integral:

$$\frac{d^q f(x)}{[d(x-a)]^q} = \frac{1}{\Gamma(n-q)} \frac{d^n}{dx^n} \int_a^x \frac{f(y)}{(x-y)^{q+1-n}} dy \quad (63)$$

Once these definitions are given, it is natural to write differential equations in terms of such quantities. In the last decade, many fractional differential equations have been proposed and solved. They include relaxation equations, wave equations, diffusion equations, etc (Mainardi [132]). In these generalizations, one replaces the usual time derivatives of integer order by fractional ones. In such a way, by varying the order of derivation, it is possible to obtain a continuous transition between completely different models of the mathematical physics. Of course, when  $q$  is not a positive integer, the fractional derivative (63) is a nonlocal operator since it depends on the lower integration limit  $a$ . The chain rule, the Leibniz rule, the composition law and other properties have been studied for fractional derivatives (Oldham and Spanier [128]). Looking for a link between fractional calculus and fractals, it is worthwhile to cite the following scaling property

(for  $a = 0$ ):

$$\frac{d^q f(bx)}{[dx]^q} = b^q \frac{d^q f(bx)}{[d(bx)]^q} \quad (64)$$

It means that the fractional differentio-integral operators are subjected to the same scaling power laws the quantities defined on fractal domains are subjected to ( $q$  being the fractal dimension). For the scaling property in the case  $a \neq 0$ , see Oldham and Spanier [128].

Recently, another important result has been achieved concerning the maximum order of fractional differentiability for nonclassical differentiable functions. Let us explain this property for two kinds of functions: the Weierstrass function and the Cantor staircase. The first one is continuous but nowhere differentiable. The singularities are locally characterized by the Hölder exponent, which is everywhere constant and equal to a certain value  $s$ ,  $0 < s < 1$ . It is possible to prove that the graph of this function is fractal with a box-counting dimension equal to  $2 - s$  and hence greater than 1. Although fractal, the Weierstrass function admits continuous fractional derivatives of order lower than  $s$ . Hence, there is a direct relationship between the fractal dimension of the graph and the maximum order of differentiability: the greater the fractal dimension, the lower the differentiability. We have already encountered a Cantor staircase in Section 3.1.2. This kind of function (Fig. 17a) can be obtained (see Feder [5]) as the integral of a constant mass density upon a lacunar fractal set belonging to the interval  $[0, 1]$ . The result is a monotonic function that grows on a fractal support; elsewhere it is constant. The devil's staircases are not fractal since they present a finite length; on the other hand, they have an infinite number of singular points characterized by a Hölder exponent equal to the fractal dimension of the support. Schellnhuber and Seyler [133] proved that the Cantor staircases admit continuous fractional derivatives of order lower than the fractal dimension of the set where they grow.

From a physical point of view, some efforts have been spent to apply space fractional differential equations to the study of phenomena involving fractal distributions in space. Here we quote Giona and Roman [134], who proposed a fractional equation to describe diffusion on fractals, and Nonnenmacher [135], who showed that a class of Lévy type processes satisfies an integral equation of fractional order. This order is also the fractal dimension of the set visited by a random walker whose jump size distribution follows the given Lévy distribution.

Recently, a new notion called *local fractional derivative* (LFD) has been introduced with the motivation of studying the local properties of fractal structures and processes (Kolwankar and Gangal [136]). The LFD definition is obtained from (63) introducing two “corrections” in order to avoid some physically undesirable features of the classical definition. In fact, if one wishes to analyze the local behaviour of a function, both the dependence on the lower limit  $a$  and the fact that adding a constant to a function yields a different fractional derivative should be avoided. This can be obtained subtracting from the function the

value of the function at the point where we want to study the local scaling property and choosing as the lower limit that point itself. Therefore, restricting our discussion to an order  $q$  comprised between 0 and 1, the LFD is defined as the following limit (if it exists and is finite):

$$D^q f(y) = \lim_{x \rightarrow y} \frac{d^q [f(x) - f(y)]}{[d(x - y)]^q}, \quad 0 < q \leq 1 \quad (65)$$

In Kolwankar and Gangal [136] it has been shown that the Weierstrass function is locally fractionally differentiable up to a *critical order*  $\alpha$  between 0 and 1. More precisely, the LFD is zero if the order is lower than  $\alpha$ , does not exist if greater, while exists and is finite only if equal to  $\alpha$ . Thus, the LFD shows a behaviour analogous to the Hausdorff measure of a fractal set. Furthermore, the critical order is strictly linked to the fractal properties of the function itself. In fact, Kolwankar and Gangal [136] showed that the critical order  $\alpha$  coincides with the local Hölder exponent  $s$  (which depends, as we have seen, on the fractal dimension), by proving the following local fractional Taylor expansion of the function  $f(x)$  of order  $q < 1$  (for  $q > 1$ , see Kolwankar and Gangal [137, 138]) for  $x \rightarrow y$ :

$$f(x) = f(y) + \frac{D^q f(y)}{\Gamma(q + 1)} (x - y)^q + R_q(x - y) \quad (66)$$

where  $R_q(x - y)$  is a remainder, negligible if compared with the other terms. Let us observe that the terms in the right hand side of Eq. (66) are nontrivial and finite only if  $q$  is equal to the critical order  $\alpha$ . Moreover, for  $q = \alpha$ , the fractional Taylor expansion (66) gives us the geometrical interpretation of the LFD. When  $q$  is set equal to unity, one obtains from (66) the equation of a tangent. All the curves passing through the same point  $y$  with the same first derivative have the same tangent. Analogously, all the curves with the same critical order  $\alpha$  and the same  $D^\alpha$  form an equivalence class modelled by  $x^\alpha$ . This is how it is possible to generalize the geometric interpretation of derivatives in terms of “tangents”.

The solution of the simple differential equation  $df/dx = 1_{[0,x]}$  gives the length of the interval  $[0, x]$ . The solution is nothing but the integral of the unit function. Wishing to extend this idea to the computation of the measure of fractal sets, it can be seen immediately that the fractional integral (62) does not work, as it fails to be additive because of its nontrivial kernel. On the other hand, Kolwankar [139] proved that a fractional measure of a fractal set can be obtained through the inverse of the LFD defined as:

$${}_a D_b^{-\alpha} f(x) = \lim_{N \rightarrow \infty} \sum_{i=0}^{N-1} f(x_i^*) \frac{d^{-\alpha} 1_{dx_i}(x)}{[d(x_{i+1} - x_i)]^{-\alpha}} \quad (67)$$

where  $[x_i, x_{i+1}]$ ,  $i = 0, \dots, N - 1$ ,  $x_0 = a$  and  $x_N = b$ , provide a partition of the interval  $[a, b]$  and  $x_i^*$  is some suitable point chosen in the subinterval  $[x_i, x_{i+1}]$ , while  $1_{dx_i}$  is the unit function defined on the same subinterval. Kolwankar called  ${}_a D_b^{-\alpha} f(x)$  the *fractal integral* of

order  $\alpha$  of  $f(x)$  over the interval  $[a, b]$ . The simple local fractional differential equation  $D^\alpha f(x) = g(x)$  has not a finite solution when  $g(x)$  is constant and  $0 < \alpha < 1$ . Interestingly, the solution exists if  $g(x)$  has a fractal support whose Hausdorff dimension  $d$  is equal to the fractional order of derivation  $\alpha$ . Consider, for instance, the triadic Cantor set  $C$ , built on the interval  $[0, 1]$ , whose dimension is  $d = \ln 2 / \ln 3$ . Let  $1_C(x)$  be the function whose value is one in the points belonging to the Cantor set upon  $[0, 1]$ , zero elsewhere. Therefore, the solution of  $D^\alpha f(x) = 1_C(x)$  when  $\alpha = d$  is  $f(x) = {}_a D_b^{-\alpha} 1_C(x)$ . Applying (67) with  $x_0 = 0$  and  $x_N = x$  and choosing  $x_i^*$  to be such that  $1_C(x_i^*)$  is maximum in the interval  $[x_i, x_{i+1}]$ , one gets (Kolwankar and Gangal [138]):

$$\begin{aligned} f(x) &= {}_0 D_x^{-\alpha} 1_C(x) = \lim_{N \rightarrow \infty} \sum_{i=0}^{N-1} F_C^i \frac{(x_{i+1} - x_i)^\alpha}{\Gamma(1 + \alpha)} \\ &= \frac{S_C(x)}{\Gamma(1 + \alpha)} \end{aligned} \quad (68)$$

where  $F_C^i$  is a flag function that takes value 1 if the interval  $[x_i, x_{i+1}]$  contains a point of the set  $C$  and 0 otherwise.  $S_C(x)$  is the Cantor (devil's) staircase (Fig. 17a), i.e. a function almost everywhere flat except on an infinite number of singular points corresponding to the underlying Cantor set where it grows from 0 to 1. Moreover, Eq. (68) introduces the *fractional measure* of a fractal set we were looking for: for the Cantor set  $C$  it is defined as  $\mathcal{F}^\alpha(C) = {}_0 D_1^{-\alpha} 1_C(x)$ . In fact  $\mathcal{F}^\alpha(C)$  is infinite if  $\alpha < d$ , and 0 if  $\alpha > d$ . For  $\alpha = d$ , we find  $\mathcal{F}^\alpha(C) = \frac{1}{\Gamma(1 + \alpha)}$ , since  $S_C(1) = 1$ . This measure definition yields the same value as the dimension predicted by the Hausdorff measure, the difference being represented only by a different value of the normalization constant. Eventually, from Eq. (68), it follows that the fractional measure of a generalized Cantor set  $C_\alpha^{[a,b]}$  of dimension  $\alpha$  built over the interval  $[a, b]$  of the  $x$ -axis is:

$$\mathcal{F}^\alpha(C_\alpha^{[a,b]}) = {}_a D_b^{-\alpha} 1_{C_\alpha^{[a,b]}}(x) = \frac{(b-a)^\alpha}{\Gamma(1 + \alpha)} \quad (69)$$

where  $1_{C_\alpha^{[a,b]}}$  is the function equal to 1 if  $x \in C_\alpha^{[a,b]}$ , to 0 elsewhere.

### 3.2.1 Size effects on tensile and flexural strength

As a first application of the local fractional operator introduced in Section 3.2, let us compute the tensile and flexural strength of a concrete specimen, for the sake of simplicity of unit thickness (Figs. 23 and 24). For load levels close to the peak, the resistant ligament  $\overline{BB'}$  is fractal-like [111]; therefore the stress field must be fractal too. Our aim is to obtain the nominal tensile and flexural strengths of a concrete beam and their size effect, under the following simplifying assumptions:

- the beam breaks when the fractal stress reaches its maximum value  $\sigma_u^*$ ;

- the resistant ligament  $\overline{BB'}$  can be modelled by a Cantor set  $C_\alpha^{[0,b]}$  of fractal dimension  $\alpha$ ,  $0 < \alpha = \frac{\ln 2}{\ln(\frac{2p}{p-1})} \leq 1$ , obtained by an iterative procedure starting from the segment  $[0, b]$  and eliminating at each step the segment fraction  $1/p$  from its middle;
- the fractal stress distributions at failure are respectively constant and linear over the ligament for tensile and bending tests:

$$\sigma^*(x) = \sigma_u^* \times 1_{C_\alpha^{[0,b]}}(x) \quad (70)$$

$$\sigma^*(x) = \left( \frac{x}{b/2} - 1 \right) \sigma_u^* \times 1_{C_\alpha^{[0,b]}}(x) \quad (71)$$

When the specimen is subjected to an axial load (fig. 23), from the previous assumptions and Eq. (69), we have that failure occurs when:

$$F_u = {}_0 D_b^{-\alpha} \left[ \sigma_u^* \times 1_{C_\alpha^{[0,b]}}(x) \right] = \frac{\sigma_u^* b^\alpha}{\Gamma(1 + \alpha)} \quad (72)$$

where  $F_u$  is the ultimate load. Assuming as responsible of the rupture the *nominal* strength  $\sigma_u = F_u/b$ , we would find that  $\sigma_u$  is no longer an exclusive property of the material but is size-dependent. In fact, from Eq. (72) we have:

$$(\sigma_u)_{tens} = \frac{\sigma_u^*}{\Gamma(1 + \alpha)} b^{-(1-\alpha)} \quad (73)$$

where we put the subscript “tens” to remind that it is the nominal strength calculated in direct tension tests. Equation (73), obtained via local fractional calculus formalism, is equivalent to Eq. 55, derived by Carpinteri [10], provided that  $1 - \alpha = d_\sigma$ .

The local fractional calculus formalism allows us to obtain also the flexural strength and its size effect (Fig. 24). In order to get the ultimate bending moment, we have to perform the integration upon the fractal ligament  $C_\alpha^{[0,b]}$  of the fractal stress distribution (71). For simple functions such as (71), fractal integrals can be obtained via mathematical series. Details can be found in Carpinteri et al. [126]. For the present case, the result is:

$$\begin{aligned} M_u &= {}_0 D_b^{-\alpha} \left[ \left( \frac{x}{b/2} - 1 \right) \sigma_u^* \times 1_{C_\alpha^{[0,b]}}(x) \right] \\ &= \frac{\sigma_u^* b^{1+\alpha}}{2 \Gamma(1 + \alpha)} \left( \frac{2^{1/\alpha} - 1}{2^{1/\alpha} + 1} \right) \end{aligned} \quad (74)$$

Notice that the ultimate bending moment increases with the size more slowly than the classical beam theory predicts ( $\sim b^2$ ). Since  $\sigma_u = 6M_u/b^2$  is the *nominal* flexural strength, a comparison with Eq. (74) yields its size effect:

$$\begin{aligned} (\sigma_u)_{flex} &= 3 \left( \frac{2^{1/\alpha} - 1}{2^{1/\alpha} + 1} \right) \frac{\sigma_u^* b^{-(1-\alpha)}}{\Gamma(1 + \alpha)} \\ &= 3 \left( \frac{2^{1/\alpha} - 1}{2^{1/\alpha} + 1} \right) (\sigma_u)_{tens} \end{aligned} \quad (75)$$

where we have used Eq. (55) and put the subscripts to distinguish the nominal strength calculated in bending

and tensile tests. The nominal flexural strength decrease with size has the same power law exponent of the tensile one (Eq. (73)); nevertheless the nominal strengths differ because of the presence in Eq. (75) of a numerical coefficient whose value varies from 1 to 3 as  $\alpha$  varies from 1 to 0. More in detail, it appears that the nominal flexural strength is always higher than the tensile one except in the Euclidean case  $\alpha = 1$ , when they are equal. While the scaling exponent is a function only of the fractal dimension of the ligament, the numerical coefficient is affected also by the fractal set describing the ligament itself. However, what is important is that, while the fractal strength  $\sigma_u^*$  is an exclusive property of the material, the nominal strength depends also on the size, as observed by Carpinteri et al. [117], as well as on the test geometry, as Eq. (75) clearly shows.

### 3.2.2 The fractal bar

In the present section, we intend to solve a simple case using the mathematical results of Section 3.2. Our aim is to show that experimental diagrams (see, for instance, Kleiser and Bocek [92]) such as the one of Fig. 17a can be obtained also analytically. More details can be found in Carpinteri and Cornetti [121].

Thus, let us consider a uniaxial model (Carpinteri and Cornetti [121]), hereafter called *fractal Cantor bar*, according to Feder's terminology [5], i.e. a bar of length  $b$  deformable on a fractal subset of dimension  $(1 - d_\varepsilon)$ . The bar axis is  $z$ . The bar is clamped in  $z = 0$ , whereas a tensile load  $N$  is applied at its end  $z = b$  (Fig. 25). A strain field will arise that is zero almost everywhere except in an infinite number of points (corresponding to the deformable subset) where it is singular. The displacement singularities can be characterized by the LFD of order equal to the fractal dimension  $\alpha = 1 - d_\varepsilon$  of the domain of the singularities, the unique value for which the LFD is finite and different from zero (the critical value). This computation is equivalent to Eq. (58), passing from the global to the local level. Therefore, we can define analytically the fractal strain  $\varepsilon^*$  as the LFD of order  $\alpha$  of the displacement:

$$\varepsilon^*(z) = D^\alpha w(z) \quad (76)$$

Let us observe that, in Eq. (76), the noninteger physical dimensions  $[L]^{d_\varepsilon}$  of  $\varepsilon^*$  are introduced by the LFD, whereas in Eq. (58) they are a geometrical consequence of the fractal dimension of the localization domain.

Without losing generality, let us assume the deformable subset to be the triadic Cantor set  $C_\alpha^{[0,b]}$  built on  $[0, b]$ ,  $\alpha = \ln 2 / \ln 3$ . In order to compute the displacement function  $w(z)$ , we need the proper constitutive law. Here, for the sake of simplicity, we use a linear elastic relation and assume  $d_\sigma = d_\varepsilon$ : in this case the coefficient of proportionality between fractal stress and fractal strain coincides with the one between the nominal quantities, i.e. it is the Young's modulus  $E$ . In symbols:  $\sigma^* = E\varepsilon^*$ .

For equilibrium reasons, the internal axial force is constant and equal to  $N$  throughout the bar. By the general-

ization of Eq. (55) to any load level and the constitutive link, we get a fractal strain  $\varepsilon^*$  equal to  $N/EA_{res}^*$  over the deformable subset, 0 elsewhere. Hence the kinematic equation (76) becomes:

$$D^\alpha w(z) = \frac{N}{EA_{res}^*} 1_{C_\alpha^{[0,b]}}(z) \quad (77)$$

Introducing the dimensionless quantities  $\tilde{w} = w/b$ ,  $\tilde{z} = z/b$  ( $\tilde{z} \in [0, 1]$ ), we can apply the scaling property expressed by Eq. (64), which is valid also for the LFD, to get  $D^\alpha w(z) = b^{1-\alpha} D^\alpha \tilde{w}(\tilde{z})$ . Eq. (77) can therefore be expressed in dimensionless form as follows:

$$D^\alpha \tilde{w}(\tilde{z}) = \frac{N}{EA_{res}^* b^{1-\alpha}} 1_C(\tilde{z}) \quad (78)$$

where  $C$  is the triadic Cantor set built on  $[0, 1]$  as indicated in Section 3.2. In this form, the solution of the differential equation (78) can be obtained directly from Eq. (68):

$$\tilde{w}(\tilde{z}) = \frac{N}{EA_{res}^* b^{1-\alpha}} \frac{S_C(\tilde{z})}{\Gamma(1 + \alpha)} \quad (79)$$

where, as explained in Section 3.2,  $S_C(x)$  is the Cantor staircase built on the interval  $[0, 1]$  and rising from 0 to 1. Recovering the physical quantities yields:

$$w(z) = \frac{Nb^*}{EA_{res}^*} S_C\left(\frac{z}{b}\right) \quad (80)$$

where  $b^* = \frac{b^\alpha}{\Gamma(1+\alpha)}$  is the fractional measure of the deformable subset. Equation (80) is plotted in fig. 25. Let us emphasize that the Cantor staircase, introduced geometrically in Section 3.1.2, is now obtained analytically. Furthermore, notice that Eq. (80) provides important information about the size effect affecting the global deformation. In fact we find that the free end displacement  $w(b)$  is equal to  $\frac{Nb^*}{EA_{res}^*}$ , i.e.  $w(b) \sim b^\alpha$ . This means that the displacement increases less than linearly with the bar length, as in the case of classical elastic bodies. From the point of view of the overall deformation  $\varepsilon = w(b)/b$ , we get  $\varepsilon \sim b^{-(1-\alpha)}$ : it decreases with size as a consequence of the strain localization on a lacunar fractal subset.

What has been done in the one-dimensional case can be formally extended in the three-dimensional case for a generic fractal medium [124]. Moreover, the finite element method can be extended also to such a medium by means of the so-called fractal splines. The interested reader is referred to [140] for further details.

### 3.3 Multifractal scaling laws

If specimens of different sizes, made of the same material, are tested in uniaxial tension, experiments show that the fractal scaling of  $\sigma_u$  and  $\mathcal{G}_F$  is strictly valid only in a limited scale range, where the fractal dimensions of the supporting domains can be considered to be constant. As the size increases, in fact, the concept of geometrical multifractality, strictly connected with the characteristics of

self-affine fractals (Carpinteri [11]), implies the progressive vanishing of fractality ( $d_\sigma \rightarrow 0$ ,  $d_G \rightarrow 0$ ) with a corresponding homogenization of the domains. Intuitively, since the microstructure of a disordered material is the same, independently of the macroscopic specimen size, the influence of disorder on the mechanical properties essentially depends on the ratio between a characteristic material length  $l_{ch}$  and the external size  $b$  of the specimen. Therefore, the effect of microstructural disorder on the mechanical behaviour of materials becomes progressively less important at the largest scales. At the smallest scales, Carpinteri [11] observed that a Brownian disorder seems to be the highest possible, yielding, respectively for invasive and lacunar morphologies, fractal scaling exponents equal to  $+1/2$  and  $-1/2$ . Notice that the stereological analysis of the concrete microstructure performed in the next Sections will agree perfectly with these values, considering them as an upper bound to concrete surface roughness and lacunarity.

On the basis of these physical and geometrical arguments, two Multifractal Scaling Laws (MFSL) have been proposed recently, respectively for fracture energy and tensile strength (Carpinteri and Chiaia [14], Carpinteri et al. [67]), which can be written in the following analytical form:

$$\mathcal{G}_F(b) = \mathcal{G}_F^\infty \left[ 1 + \frac{l_{ch}}{b} \right]^{-1/2} \quad (81)$$

$$\sigma_u(b) = f_t \left[ 1 + \frac{l_{ch}}{b} \right]^{1/2} \quad (82)$$

These scaling laws are both two-parameters models, where the asymptotic value of the nominal quantity ( $\mathcal{G}_F^\infty$  or  $f_t$ ), corresponding respectively to the highest nominal fracture energy and to the lowest nominal tensile strength, is reached only in the limit of infinite sizes. The dimensionless term into square brackets, which is controlled by the characteristic length  $l_{ch}$ , represents the variable influence of disorder on the mechanical behaviour. Note the perfect similitude between the two scaling laws, where the only difference is the sign of the Brownian exponent,  $\pm 1/2$ , respectively related to an invasive or to a lacunar topology. In the bilogarithmic diagrams, shown in Fig. 26, the transition from the fractal scaling regime to the Euclidean one is evident, the transition scale being represented by the point of abscissa  $\ln l_{ch}$ .

The scaling behaviour of the kinematical parameters shows that the critical nominal strain  $\varepsilon_c$  decreases as the bar length increases – see Eq. (58). As shown analytically in Section 3.2.2, by increasing the size, the bar progressively loses its deformation capacity (or ductility) and tends to a more brittle behaviour. For a given material, the fractal exponent  $d_\varepsilon$  increases with the size of the bar, from the value  $d_\varepsilon = 0$  (homogeneous deformation) to  $d_\varepsilon = 1$  (highly localized deformation). In the limit of very large and very small sizes, the collapse kinematics will be ruled respectively by a pure opening displacement ( $w_c^\infty$ ) of a single crack or by a pure dilation ( $\varepsilon_c^0$ ).

The displacement diagrams corresponding to the two limit cases are reported in Fig. 27. In the case of short bars, the elongation is linearly increasing along the bar (Fig. 27a). In the case of long bars, strain develops only in correspondence of one (or a finite number of) cross-section where the displacement presents a sharp discontinuity, resembling a step function (Fig. 27b). The intermediate case is represented by the Cantor staircase plot of Fig. 17a, analyzed in the previous section. In the limit cases of extremely short or extremely long bars, the critical fractal strain  $\varepsilon_c^*$  holds respectively the physical dimension of a canonical strain ( $[L]^0$ ) or that of a displacement ( $[L]^1$ ). In other words, the collapse occurs at small scales when the strain  $\varepsilon$  attains its limit value ( $\varepsilon_c^0$ ), whereas, at large scales, when a threshold value  $w_c^\infty$  for the displacement  $w$  is reached; in the intermediate situations, when the anomalous ratio between displacement and length of the bar raised to a fractal exponent ( $w_c/b^{1-d_\varepsilon}$ ) reaches its critical value  $\varepsilon_c^*$ .

In perfect analogy with the MFSLs for tensile strength and fracture energy – see Eqs. (81) and (82) – a new Multifractal Scaling Law can be proposed for the critical strain  $\varepsilon_c$ . The lack of complete similarity implies that an internal length  $l_{ch}$  is present also in the kinematics of damage. Thereby, the previous (monofractal) scaling relation (58) has to be modified by considering the exponent  $d_\varepsilon$  smoothly variable with the structural size. Since the influence of microstructural disorder is higher for smaller sizes, it seems reasonable to put  $d_\varepsilon$  equal to zero for very short bars (maximum disorder, that is, damage diffused throughout the volume, corresponding to ductile behaviour), and  $d_\varepsilon = 1$  for very long bars (maximum order, that is, localization of fracture on a single cross-section, corresponding to brittle behaviour). If the critical strain  $\varepsilon_c$  is plotted vs. the bar length  $b$  in the bilogarithmic diagram, two asymptotes are revealed. The first, valid for  $b \rightarrow 0$ , is horizontal, i.e. no size effect affects  $\varepsilon_c$  for very short bars ( $d_\varepsilon = 0$ ). The second, valid for very long bars ( $b \rightarrow \infty$ ), presents a  $-45^\circ$  slope, corresponding to the maximum size effect ( $d_\varepsilon = 1$ ) on  $\varepsilon_c$ . The Multifractal Scaling Law for the critical strain can thus be written as:

$$\varepsilon_c(b) = \varepsilon_c^0 \left[ 1 + \frac{b}{l_{ch}} \right]^{-1} \quad (83)$$

where  $\varepsilon_c^0$  is the asymptotic value of the critical strain, valid for the smallest sizes, and  $l_{ch}$  is the characteristic length, depending on the material microstructure and on the test geometry. Eq. (83) can be expressed equivalently in terms of critical displacement:

$$w_c(b) = w_c^\infty \left[ 1 + \frac{l_{ch}}{b} \right]^{-1} \quad (84)$$

provided that  $\varepsilon_c^0 = w_c^\infty / l_{ch}$ . In a bilogarithmic plot, the critical displacement increases with a unit slope at the smallest sizes, while becomes constant at the largest ones. Together with Eqs. (81) and (82), Eq. (84) completes

the description of the size effects upon the cohesive law parameters.

Equation (83), plotted in Fig. 28, closely resembles (apart from the large-size slope) Bažant’s size effect law for strength (Bažant[141]). Even if the physical assumptions are very different, it is interesting to observe some similarities between the two scaling laws. The horizontal asymptote for small sizes, for example, is provided by an intrinsic limit strength in the case of Bažant’s law and by an intrinsic limit strain in Eq. (83). Both assumptions can be traced to classical continuum mechanics arguments. In addition, both the nominal strength, according to Bažant’s law, and the nominal ultimate strain, according to the MFSL, tend to zero for very large sizes. This is due, in both cases, to localization, i.e. to a collapse governed by Fracture Mechanics. On the other hand, in the case of Bažant’s law, this trend is physically sound only for geometrically similar notched structures, whereas, in the case of unnotched structures, a constant limit strength is attained for very large sizes – see Eq. (82).

In conclusion, the fundamental relation among the three fractional exponents, Eq. (61), specialized at the various scales, can be written as:

$$\text{MACROSCALE} : d_\sigma \cong d_G \cong 0, \quad d_\varepsilon \cong 1 \quad (85)$$

$$\text{MESOSCALE} : d_\varepsilon + d_\sigma + d_G = 1 \quad (86)$$

$$\text{MICROSCALE} : d_\sigma \cong d_G \cong 1/2, \quad d_\varepsilon \cong 0 \quad (87)$$

equation (61) being valid in all cases. The three MFSLs (81), (82) and (84) for extremely small structures ( $b \rightarrow 0$ ) become respectively:

$$\mathcal{G}_F = \frac{\mathcal{G}_F^\infty}{\sqrt{l_{ch}}} b^{1/2}, \quad \sigma_u = (f_t \sqrt{l_{ch}}) b^{-1/2}, \quad w_c = \frac{w_c^\infty}{l_{ch}} b \quad (88)$$

A comparison between these expressions and Eqs. (57), (55), (58) leads to:

$$\mathcal{G}_F^* = \frac{\mathcal{G}_F^\infty}{\sqrt{l_{ch}}}, \quad \sigma_u^* = f_t \sqrt{l_{ch}}, \quad \varepsilon_c^* = \frac{w_c^\infty}{l_{ch}} \quad (89)$$

the scaling exponents being given by Eq. (87). Eqs. (89) point out the link between the scale-invariant parameters governing concrete tensile failure at extremely small and large scales.

In order to summarize all the above remarks, the limit values of the scaling exponents and of the scale-invariant parameters  $\varepsilon_c^*$ ,  $\sigma_u^*$ ,  $\mathcal{G}_F^*$  are concisely described in table 1. Observe that at large scales they coincide with the cohesive law parameters, i.e. the critical crack opening displacement, the tensile strength and the fracture energy, whereas at small scales their physical dimensions change, because of the presence of a power of the characteristic material length.

## References

- [1] K.G. Wilson. Renormalization group and critical phenomena. *Physical Review*, 4:3174–3205, 1971.
- [2] H.J. Herrmann and S. Roux. *Statistical Models for the Fracture of Disordered Media*. North-Holland, Amsterdam, 1990.
- [3] K.R. Popper. *The Logic of Scientific Discovery*. Hutchinson, London, 1968.
- [4] A. Carpinteri. Decrease of apparent tensile and bending strength with specimen size: two different explanations based on fracture mechanics. *International Journal of Solids and Structures*, 25:407–429, 1989.
- [5] J. Feder. *Fractals*. New York: Plenum Press, 1988.
- [6] B.B. Mandelbrot. *The Fractal Geometry of Nature*. W. H. Freeman & Company, New York, 1982.
- [7] K. Falconer. *Fractal Geometry: Mathematical Foundations and Applications*. John Wiley & Sons, Chichester, 1990.
- [8] B.B. Mandelbrot, D.E. Passoja, and A.J. Paullay. Fractal character of fractal surfaces of metals. *Nature*, 308:721–722, 1984.
- [9] V.E. Saouma, C.C. Barton, and N.A. Gamaleldin. Fractal characterization of fracture surfaces in concrete. *Engineering Fracture Mechanics*, 35:47–53, 1990.
- [10] A. Carpinteri. Fractal nature of material microstructure and size effects on apparent mechanical properties. *Mechanics of Materials*, 18:89–101, 1994.
- [11] A. Carpinteri. Scaling laws and renormalization groups for strength and toughness of disordered materials. *International Journal of Solids and Structures*, 31:291–302, 1994.
- [12] A. Carpinteri and G. Ferro. Size effects on tensile fracture properties: a unified explanation based on disorder and fractality of concrete microstructure. *Materials and Structures*, 28:563–571, 1994.
- [13] A. Carpinteri, G. Ferrara, and L. Imperato. Scaling law for strength and toughness of disordered materials: a unified theory based on fractal geometry. *Engineering Fracture Mechanics*, 48:673–689, 1994.
- [14] A. Carpinteri and B. Chiaia. Multifractal nature of concrete fracture surfaces and size effects on nominal fracture energy. *Materials and Structures*, 28:435–443, 1995.
- [15] A. Carpinteri, B. Chiaia, and F. Maradei. Experimental determination of the fractal dimension of disordered fracture surfaces. In A. Carpinteri G.C. Sih and G. Surace, editors, *Advanced Technology for Design and Fabrication of Composite Materials and Structures*, pages 269–292. Kluwer Academic Publishers, Dordrecht, The Netherlands, 1995.
- [16] A.A. Griffith. The phenomena of rupture and flow in solids. *Philosophical Transaction of the Royal Society*, A221:163–198, 1921.
- [17] J.A. Begley and J.D. Landes. The j-integral as a fracture criterion. *ASTM, Special Technical Publication*, 514:1–23, 1972.
- [18] E. Buckingham. Model experiments and the form of empirical equations. *ASME Transactions*, 37:263–296, 1915.
- [19] A. Carpinteri. Notch sensitivity in fracture testing of aggregative materials. *Engineering Fracture Mechanics*, 16:467–481, 1982.
- [20] A. Carpinteri. Static and energetic fracture parameters for rocks and concretes. *Materials and Structures*, 14:151–162, 1981.

- [21] A. Carpinteri. Interpretation of the Griffith instability as a bifurcation of the global equilibrium. In S.P. Shah, editor, *N.A.T.O. Advanced Research Workshop on Application of Fracture Mechanics to Cementitious Composites*, pages 284–316, The Netherlands, 1985. Martinus Nijhoff.
- [22] A. Carpinteri. Size effects on strength, toughness and ductility. *Journal of Engineering Mechanics (ASCE)*, 115:1375–1392, 1989.
- [23] A. Carpinteri. Cusp catastrophe interpretation of fracture instability. *Journal of Mechanics and Physics of Solids*, 37: 567–582, 1989.
- [24] G.I. Barenblatt. *Similarity, Self-Similarity and Intermediate Asymptotics*. Consultants Bureau, New York, 1979.
- [25] Standard method of test for plane strain fracture toughness of metallic materials. Technical Report E399-74, A.S.T.M.
- [26] A. Carpinteri. Size effect in fracture toughness testing: a dimensional analysis approach. In G.C. Sih and M. Mirabile, editors, *Conference on Analytical and Experimental Fracture Mechanics*, pages 785–797, Rome, Italy, 1980. Sijthoff and Noordhoff.
- [27] A. Carpinteri. Application of fracture mechanics to concrete structures. *Journal of Engineering Mechanics (ASCE)*, 108: 833–848, 1982.
- [28] H. Tada, P. Paris, and G. Irwin. *The Stress Analysis of Cracks Handbook*. Del Research Corporation, St. Louis (Missouri), 1963.
- [29] G.I. Barenblatt. The formation of equilibrium cracks during brittle fracture: general ideas and hypotheses. *Journal of Applied Mathematics and Mechanics*, 23:622–636, 1959.
- [30] G.I. Barenblatt. The mathematical theory of equilibrium cracks in brittle fracture. *Advances in Applied Mechanics*, 7:55–129, 1962.
- [31] D.S. Dugdale. Yielding of steel sheets containing slits. *Journal of Mechanics and Physics of Solids*, 8:100–114, 1960.
- [32] B.A. Bilby, A.H. Cottrell, and K.H. Swinden. The spread of plastic yield from a notch. In *Proceedings of the Royal Society*, volume A272, pages 304–314, 1963.
- [33] J.R. Rice. A path independent integral and the approximate analysis of strain concentration by notches and cracks. *Journal of Applied Mechanics*, 15:379–386, 1968.
- [34] J.R. Willis. A comparison of the fracture criteria of Griffith and Barenblatt. *Journal of Mechanics and Physics of Solids*, 15:151–162, 1967.
- [35] M.P. Wnuk. Quasi-static extension of a tensile crack contained in viscoelastic-plastic solid. *Journal of Applied Mechanics*, 41:234–242, 1974.
- [36] A. Hillerborg, M. Modeer, and P.E. Petersson. Analysis of crack formation and crack growth in concrete by means of fracture mechanics and finite elements. *Cement and Concrete Research*, 6:773–782, 1976.
- [37] A. Carpinteri, A. Di Tommaso, and M. Fanelli. Influence of material parameters and geometry on cohesive crack propagation. In F.H. Wittmann, editor, *Fracture Toughness and Fracture Energy of Concrete*, pages 117–135. Elsevier Science Publisher, 1985.
- [38] P.E. Petersson. Crack growth and development of fracture zones in plain concrete and similar materials. In *Report TVBM-1006*, Division of Building Materials, Lund Institute of Technology, Denmark, 1981.
- [39] M. Wecharatana and S.P. Shah. Prediction of non-linear fracture process zone in concrete. *Journal of Engineering Mechanics (ASCE)*, 109:1231–1246, 1983.
- [40] Z.P. Bažant and B.H. Oh. Concrete fracture via stress-strain relations. Technical Report 81-10/665c, Center for Concrete and Geomaterials, Northwestern University, 1981.
- [41] A.R. Ingraffea and W.H. Gerstle. Nonlinear fracture models for discrete crack propagation. In S.P. Shah, editor, *N.A.T.O. Advanced Research Workshop on Application of Fracture Mechanics to Cementitious Composites*, pages 171–209, The Netherlands, 1985. Martinus Nijhoff.
- [42] A. Carpinteri. Post-peak and post-bifurcation analysis on cohesive crack propagation. *Engineering Fracture Mechanics*, 32:265–278, 1989.
- [43] A. Carpinteri, G. Colombo, and G. Giuseppetti. Accuracy of the numerical description of cohesive crack propagation. In F.H. Wittmann, editor, *Fracture Toughness and Fracture Energy of Concrete*, pages 189–195. Elsevier Science Publisher, 1985.
- [44] A. Carpinteri, A. Di Tommaso, G. Ferrara, and G. Melchiorri. Experimental evaluation of concrete fracture energy through a new identification method. In F.H. Wittmann, editor, *Fracture Toughness and Fracture Energy of Concrete*, pages 423–436. Elsevier Science Publisher, 1985.
- [45] A. Carpinteri and S. Valente. Numerical modeling of mixed-mode cohesive crack propagation. In S.N. Atluri and G. Yagawa, editors, *International Conference on Computational Engineering Science*, pages 12.vi.1–12.vi.2. Springer Verlag, 1988.
- [46] Z. Cen and G. Maier. Bifurcations and instabilities in fracture of cohesive-softening structures: a boundary elements analysis. *Fatigue and Fracture of Engineering Materials and Structures*, 15:911–928, 1992.
- [47] M. Elices, G.V. Guinea, and J. Planas. Prediction of size-effect based on cohesive crack model. In A. Carpinteri, editor, *Size-Scale Effects in the Failure Mechanisms of Materials and Structures*, pages 309–324. E&FN Spon, 1996.
- [48] M. Elices, G.V. Guinea, J. Gomez, and J. Planas. The cohesive zone model: advantages, limitations and challenges. *Engineering Fracture Mechanics*, 69:137–163, 2002.
- [49] J. Planas, G.V. Guinea, and M. Elices. Size effect and inverse analysis in concrete fracture. *International Journal of Fracture*, 95:367–378, 1999.
- [50] Z.P. Bažant. Concrete fracture models: testing and practice. *Engineering Fracture Mechanics*, 69:165–205, 2002.
- [51] A. Carpinteri and G. Ferro. Fracture assessment in concrete structures. In R.A. Ainsworth and K.H. Schwalbe, editors, *Comprehensive Structural Integrity*, pages 501–528, Amsterdam, Holland, 2003. Elsevier Applied Science.
- [52] M.G.A. Tijssens. *On the Cohesive Surface Methodology for Fracture of Brittle Heterogeneous Solids*. PhD thesis, Technical University of Delft (The Netherlands), 2000.
- [53] M.G.A. Tijssens, E. van der Giessen, and L.J. Sluys. Simulation of mode I crack growth in polymers by crazing. *International Journal of Solids and Structures*, 37:7307–7327, 2000.
- [54] A. Needleman. A continuum model for void nucleation by inclusion debonding. *Journal of Applied Mechanics*, 54:525–531, 1987.

- [55] A. Needleman. An analysis of tensile decohesion along an interface. *Journal of Mechanics and Physics of Solids*, 38: 289–324, 1990.
- [56] V. Tvergaard and J.W. Hutchinson. The relation between crack growth resistance and fracture process parameters in elastic–plastic solids. *Journal of Mechanics and Physics of Solids*, 40:1377–1397, 1992.
- [57] V. Tvergaard and J.W. Hutchinson. Effect of T-stress on mode I crack growth resistance in a ductile solid. *International Journal of Solids and Structures*, 31:823–833, 1994.
- [58] V. Tvergaard and J.W. Hutchinson. Toughness of an interface along a thin ductile layer joining elastic solids. *Philosophical Magazine A*, 70:641–656, 1994.
- [59] V. Tvergaard. Resistance curves for mixed mode interface crack growth between dissimilar elastic–plastic solids. *Journal of Mechanics and Physics of Solids*, 49:2689–2703, 2001.
- [60] G. Lin. *Numerical Investigation of Crack Growth Behaviour Using a Cohesive Zone Model*. PhD thesis, University of Hamburg-Harburg, Geesthacht (Germany), 1998.
- [61] G. Lin, A. Cornec, and K.H. Schwalbe. Three-dimensional finite element simulation of crack extension in aluminium alloy 2024-FC. *Fatigue and Fracture of Engineering Materials and Structures*, 21:1159–1173, 1998.
- [62] G. Lin, X.G. Meng, A. Cornec, and K.H. Schwalbe. The effect of strength mismatch on mechanical performance of weld joints. *International Journal of Fracture*, 96:37–54, 1999.
- [63] X.P. Xu and A. Needleman. Numerical simulations of fast crack growth in brittle solids. *Journal of Mechanics and Physics of Solids*, 42:1397–1434, 1994.
- [64] P.D. Zavattieri and H.D. Espinosa. Grain level analysis of crack initiation and propagation in brittle materials. *Acta Materialia*, 49:4291–4311, 2001.
- [65] D.H. Allen and C.R. Searcy. A micromechanical model for a viscoelastic cohesive zone. *International Journal of Fracture*, 107:159–176, 2001.
- [66] V.S. Deshpande, A. Needleman, and E. van der Giessen. A discrete dislocation analysis of near-threshold fatigue crack growth. *Acta Materialia*, 49:3189–3203, 2001.
- [67] A. Carpinteri, B. Chiaia, and G. Ferro. Size effects on nominal tensile strength of concrete structures: multifractality of material ligaments and dimensional transition from order to disorder. *Materials and Structures*, 28:311–317, 1995.
- [68] A. Carpinteri, B. Chiaia, and P. Cornetti. A scale-invariant cohesive crack model for quasi-brittle materials. *Engineering Fracture Mechanics*, 69:207–217, 2002.
- [69] J. G. M. Van Mier and M. R. A. Van Vliet. Effect of strain gradients on the size effect of concrete in uniaxial tension. *International Journal of Fracture*, 94:195–219, 1999.
- [70] A. Carpinteri. Nonlinear phenomena associated with fracture in strain-softening materials. In M.P. Wnuk, editor, *Non-linear Fracture Mechanics*, pages 61–121. Springer Verlag, Wien, 1990.
- [71] G. Colombo and E. Limido. A numerical method for the analysis of stable T.P.B.T. test: comparison with some experimental data. In *XI Convegno Nazionale per l'Analisi delle Sollecitazioni*, pages 233–243, Turin, 1983.
- [72] P. Bocca, A. Carpinteri, and S. Valente. Fracture mechanics of brick masonry: size effect and snap-back analysis. *Materials and Structures*, 22:364–373, 1989.
- [73] Determination of the fracture energy of mortar and concrete by means of three-point bending tests on notched beams. Technical Report 18, Materials and Structures (R.I.L.E.M.), 1985.
- [74] G. Maier, Z. Cen, G. Novati, and R. Tagliaferri. Fracture, path bifurcations and instabilities in elastic cohesive-softening models: a boundary elements approach. In J.G.M. van Mier, J.G. Rots, and A. Bakker, editors, *Fracture Processes in Concrete, Rock, Ceramics*, pages 695–704. E&FN Spon, 1991.
- [75] C. Fairhurst, J.A. Hudson, and E.T. Brown. Optimizing the control of rock failure in servo-controlled laboratory test. *Rock Mechanics*, 3:217–224, 1971.
- [76] K. Rokugo, K. Ohno, and W. Koyanagi. Automatical measuring system of load-displacement curves including post-failure region of concrete specimens. In *Fracture Toughness and Fracture Energy of Concrete – International Conference of Fracture Mechanics of Concrete*, Lausanne, Switzerland, 1986.
- [77] L. Biolzi, S. Cangiano, G.P. Tognon, and A. Carpinteri. Snap-back softening instability in high strength concrete beams. *Materials and Structures*, 22:429–436, 1989.
- [78] A. Carpinteri and G.C. Sih. Damage accumulation and crack growth in bilinear materials with softening. *Theoretical and Applied Fracture Mechanics*, 1:145–159, 1984.
- [79] L. Cedolin, S. Dei Poli, and I. Iori. Tensile behaviour of concrete. *Journal of Engineering Mechanics (ASCE)*, 113: 431–449, 1987.
- [80] B. Barr and T.J. Bear. Fracture toughness tests for concrete. *International Journal of Fracture*, 13:92–96, 1977.
- [81] A.R. Ingraffea and V. Saouma. Numerical modeling of discrete crack propagation in plain and reinforced concrete. In G.C. Sih and A. Di Tommaso, editors, *Fracture Mechanics of Concrete: Structural Application and Numerical Calculation*, pages 171–225. Martinus Nijhoff Publishers, 1985.
- [82] J. Kasperkiewicz, D. Dalhuisen, and P. Stroeven. Structural effects in the fracture of concrete. In A.M. Brandt and I.H. Marshall, editors, *Brittle matrix composites 1*, pages 537–548. Elsevier Applied Science, 1986.
- [83] V.C. Li and E. Liang. Fracture processes in concrete and fiber reinforced cementitious composites. *Journal of Engineering Mechanics (ASCE)*, 112:566–586, 1986.
- [84] V.C. Li, C.M. Chan, and K.Y. Leung. Experimental determination of the tension-softening relations for cementitious composites. *Cement and Concrete Research*, 17:441–452, 1987.
- [85] S.P. Shah. Dependence of concrete fracture toughness on specimen geometry and on composition. In A. Carpinteri and A.R. Ingraffea, editors, *Fracture Mechanics of Concrete: Material Characterization and Testing*, pages 135–115. Martinus Nijhoff Publishers, 1984.
- [86] P.F. Walsh. Fracture of plain concrete. *Indian Concrete Journal*, 44:469–470, 1972.
- [87] Y.V. Zaitsev and K.L. Kovler. Effect of specimen geometry, stress state and structure heterogeneity of cementitious composite materials on  $K_{IC}$ . In A.M. Brandt and I.H. Marshall, editors, *Brittle matrix composites 1*, pages 559–570. Elsevier Applied Science, 1986.
- [88] S. Ziegeldorf, H.S. Muller, and H.K. Hilsdorf. A model law for the notch sensitivity of brittle materials. *Cement and Concrete Research*, 10:589–599, 1987.

- [89] A. Carpinteri and S. Valente. Size-scale transition from ductile to brittle fracture: a dimensional analysis approach. In J. Mazars and Z.P. Bažant, editors, *Cracking and Damage - Strain-Localization and Size Effect*, pages 477–490. Elsevier Applied Science, 1989.
- [90] B.B. Mandelbrot. *The Fractal Geometry of Nature*. W.H. Freeman and Company, San Francisco, 1983.
- [91] B.B. Maier, D.E. Passoja, and A.J. Paullay. Fractal character of fracture surfaces of metals. *Nature*, 308:721–722, 1984.
- [92] T. Kleiser and M. Bocek. The fractal nature of slip in crystals. *Zeitschrift für Metallkunde*, 77:582–587, 1986.
- [93] R.H. Dauskardt, F. Haubensak, and R.O. Ritchie. On the interpretation of the fractal character of fracture surfaces. *Acta Metallica Materialia*, 38:143–159, 1990.
- [94] E. Charkaluk, M. Bigerelle, and A. Iost. Fractals and fracture. *Engineering Fracture Mechanics*, 61:119–139, 1998.
- [95] A. Carpinteri, B. Chiaia, and P. Cornetti. On the mechanics of quasi-brittle materials with a fractal microstructure. *Engineering Fracture Mechanics*, 70:2321–2349, 2003.
- [96] A. Carpinteri, P. Cornetti, and S. Puzzi. A stereological analysis of aggregate grading and size effect on concrete tensile strength. *International Journal of Fracture*, 128:233–242, 2004.
- [97] V.E. Panin, T.F. Elsukova, G.V. Angelova, and P.V. Kuznetsov. Mechanism of formation of fractal mesostructure at the surface of polycrystals upon cyclic loading. *The Physics of Metals and Metallography*, 94:402–412, 2002.
- [98] A. Mosolov. Multifractal fracture and size effect. *Fractals*, 2: 5–8, 1994.
- [99] F.M. Borodich. Some fractal models of fracture. *Journal of Mechanics and Physics of Solids*, 45:239–259, 1997.
- [100] A.S. Balankin. Physics of fracture and mechanics of self affine cracks. *Engineering Fracture Mechanics*, 57:135–203, 1997.
- [101] P.D. Panagiotopoulos. Fractal geometry in solids and structures. *International Journal of Solids and Structures*, 29: 2159–2175, 1992.
- [102] A. Yavari, S. Sarkani, and E.T. Moyer Jr. The mechanics of self-similar and self-affine fractal cracks. *International Journal of Fracture*, 114:1–27, 2002.
- [103] S. Stach, J. Cybo, and J. Chmiela. Fracture surface - fractal or multifractal? *Materials Characterization*, 46:163–167, 2001.
- [104] D.N. Winslow. The fractal nature of the surface of cement paste. *Cement and Concrete Research*, 15:817–824, 1985.
- [105] Mo.A. Issa, Ma.A. Issa, Md.S. Islam, and A. Chudnovsky. Fractal dimension - a measure of fracture roughness and toughness of concrete. *Engineering Fracture Mechanics*, 70: 125–137, 2003.
- [106] A. Carpinteri, P. Cornetti, F. Barpi, and S. Valente. Cohesive crack model description of ductile to brittle size-scale transition: dimensional analysis vs. renormalization group theory. *Engineering Fracture Mechanics*, 70:1809–1839, 2003.
- [107] Z.P. Bažant, J.K. Kim, and P.A. Pfeiffer. Determination of fracture properties from size effect tests. *Journal of Structural Engineering (ASCE)*, 112:289–307, 1984.
- [108] J. G. M. Van Mier and M. R. A. Van Vliet. Experimental investigation of size effect in concrete under uniaxial tension. In H. Mihashi and K. Rokugo, editors, *Proceedings of "FRAMCOS-3"*, pages 1923–1936. AEDIFICATIO, 1998.
- [109] A. Carpinteri, B. Chiaia, and K.M. Nemati. Complex fracture energy dissipation in concrete under different loading conditions. *Mechanics of Materials*, 26:93–108, 1997.
- [110] A. Carpinteri, B. Chiaia, and S. Invernizzi. Three-dimensional fractal analysis of concrete fracture at the meso-level. *Theoretical and Applied Fracture Mechanics*, 31:163–172, 1999.
- [111] A. Carpinteri and P. Cornetti. Size effects on concrete tensile fracture properties: an interpretation of the fractal approach based on the aggregate grading. *Journal of the Mechanical Behavior of Materials*, 13:233–246, 2002.
- [112] A. Carpinteri and B. Chiaia. Power scaling laws and dimensional transitions in solid mechanics. *Chaos, Solitons and Fractals*, 7:1343–1364, 1996.
- [113] A. Carpinteri and B. Chiaia. Multifractal scaling laws in the breaking behavior of disordered materials. *Chaos, Solitons and Fractals*, 8:135–150, 1997.
- [114] A. Carpinteri, B. Chiaia, and G. Ferro. Scale dependence of tensile strength of concrete specimens: a multifractal approach. *Magazine of Concrete Research*, 50:237–246, 1998.
- [115] A. Carpinteri and B. Chiaia. Size effects on concrete fracture energy: dimensional transition from order to disorder. *Materials and Structures*, 29:259–266, 1996.
- [116] A. Carpinteri and B. Chiaia. Crack-resistance behavior as a consequence of self-similar fracture topologies. *International Journal of Fracture*, 76:327–340, 1996.
- [117] A. Carpinteri, B. Chiaia, and G. Ferro. A new explanation for size effects on the flexural strength of concrete. *Magazine of Concrete Research*, 49:45–53, 1997.
- [118] A. Carpinteri, G. Ferro, and I. Monetto. Scale effects in uniaxially compressed concrete specimens. *Magazine of Concrete Research*, 51:217–225, 1999.
- [119] A. Konstantinidis, G. Frantziskonis, A. Carpinteri, and E.C. Aifantis. Size effects on tensile strength and fracture energy in concrete: wavelet vs. fractal approach. *Journal of Mechanical Behaviour of Materials*, 12:63–75, 2001.
- [120] G. Efraimidis, A. Carpinteri, and E.C. Aifantis. Multifractal scaling law versus gradient elasticity in the evaluation of disordered materials compressive strength. *Journal of Mechanical Behaviour of Materials*, 12:107–120, 2001.
- [121] A. Carpinteri and P. Cornetti. A fractional calculus approach to the description of stress and strain localization in fractal media. *Chaos, Solitons and Fractals*, 13:85–94, 2002.
- [122] A. Carpinteri and F. Mainardi, editors. *Fractals and Fractional Calculus in Continuum Mechanics*. Springer-Verlag, Wien, 1997.
- [123] K. M. Kolwankar. *Studies of Fractal Structures and Processes Using Methods of Fractional Calculus*. PhD thesis, University of Pune, 1998.
- [124] A. Carpinteri, B. Chiaia, and P. Cornetti. Static-kinematic duality and the principle of virtual work in the mechanics of fractal media. *Computer Methods in Applied Mechanics and Engineering*, 191:3–19, 2001.
- [125] A. Carpinteri, B. Chiaia, and P. Cornetti. A fractional calculus approach to the mechanics of fractal media. *Zeitschrift für Angewandte Mathematik und Mechanik*, 84:128–135, 2004.
- [126] A. Carpinteri, P. Cornetti, and K. M. Kolwankar. Calculation of the tensile and flexural strength of disordered materials using fractional calculus. *Chaos, Solitons and Fractals*, 21: 623–632, 2004.

- [127] A. Carpinteri and G. Ferro. Scaling behaviour and dual renormalization of experimental tensile softening responses. *Materials and Structures*, 31:303–309, 1998.
- [128] K. B. Oldham and J. Spanier. *The Fractional Calculus*. Academic Press, New York, 1974.
- [129] K. S. Miller and B. Ross. *An Introduction to the Fractional Calculus and Fractional Differential Equations*. Wiley, New York, 1993.
- [130] S. G. Samko, A. A. Kilbas, and O. I. Marichev. *Fractional Integrals and Derivatives: Theory and Applications*. Gordon & Breach, Amsterdam, 1993.
- [131] I. Podlubny. *Fractional Differential Equations*. Academic Press, San Diego, 1999.
- [132] F. Mainardi. Fractional relaxation-oscillation and fractional diffusion-wave phenomena. *Chaos, Solitons and Fractals*, 7: 1461–1477, 1996.
- [133] H. J. Schellnhuber and A. Seyler. Fractional differentiation of devil’s staircases. *Physica A*, 191:491–500, 1992.
- [134] M. Giona and H. E. Roman. Fractional diffusion equation on fractals: one-dimensional case and asymptotic behavior. *Journal of Physics A*, 25:2093–2105, 1992.
- [135] T. F. Nonnenmacher. Fractional integral and differential equations for a class of Lévy-type probability densities. *Journal of Physics A*, 23:L697–L700, 1990.
- [136] K. M. Kolwankar and A. D. Gangal. Fractional differentiability of nowhere differentiable functions and dimensions. *Chaos*, 6:505–523, 1996.
- [137] K. M. Kolwankar and A. D. Gangal. Hölder exponents of irregular signals and local fractional derivatives. *Pramana Journal of Physics*, 48:49–68, 1997.
- [138] K. M. Kolwankar and A. D. Gangal. Local fractional Fokker-Planck equation. *Physical Review Letters*, 80:214–217, 1998.
- [139] K. M. Kolwankar and A. D. Gangal. Local fractional calculus: a calculus for fractal space-time. In *Proceedings of “Fractals: Theory and Applications in Engineering”*, pages 171–181, Delft, The Netherlands, 1999. Springer.
- [140] A. Carpinteri, B. Chiaia, and P. Cornetti. The elastic problem for fractal media: basic theory and finite element formulation. *Computers and Structures*, 82:499–508, 2004.
- [141] Z.P. Bažant. Size effect in blunt fracture: concrete, rock, metal. *Journal of Engineering Mechanics (ASCE)*, 110:518–535, 1984.
- [142] G. Ferro. *Effetti di Scala sulla Resistenza a Trazione dei Materiali*. PhD thesis, Politecnico di Torino, 1994.
- [143] M. R. A. Van Vliet. *Size Effect in Tensile Fracture of Concrete and Rock*. PhD thesis, Technical University of Delft, 2000.

# List of Tables

1 Values of the scaling exponents and of the size- independent material parameters for extremely small or large structures. . . . . 25

SMALL STRUCTURES Fractal Damage			LARGE STRUCTURES Fracture Mechanics		
$d_\varepsilon = 0$	$d_\sigma = 1/2$	$d_G = 1/2$	$d_\varepsilon = 1$	$d_\sigma = 0$	$d_G = 0$
Diffused damage. Uniform strain in the bulk. Ductility.	Fractal lacunar resisting cross-section at the peak load.	Energy dissipated on a fractal invasive domain.	Damage localized on a finite number of cross-sections. Brittleness.	Two-dimensional resisting cross-section.	Energy dissipated on localized surfaces.
$\varepsilon_c^* = \frac{w_c^\infty}{l_{ch}}$ [L] <sup>0</sup>	$\sigma_u^* = f_t \sqrt{l_{ch}}$ [F][L] <sup>-1.5</sup>	$\mathcal{G}_F^* = \frac{\mathcal{G}_F^\infty}{\sqrt{l_{ch}}}$ [FL][L] <sup>-2.5</sup>	$\varepsilon_c^* = w_c^\infty$ [L]	$\sigma_u^* = f_t$ [F][L] <sup>-2</sup>	$\mathcal{G}_F^* = \mathcal{G}_F^\infty$ [FL][L] <sup>-2</sup>

Table 1: Values of the scaling exponents and of the size-independent material parameters for extremely small or large structures.

# List of Figures

1	Dimensionless load of crack instability versus relative crack depth . . . . .	28
2	Dimensionless load of crack instability as a function of the dimensionless deflection . . . . .	29
3	Dimensionless load of crack instability versus dimensionless crack mouth opening displacement . . . . .	30
4	Constitutive laws of the cohesive crack model: (a) undamaged material, (b) process zone. . . . .	31
5	Limit-situation of complete fracture with cohesive forces . . . . .	32
6	Load-deflection diagrams: (a) ductile and (b) brittle condition. . . . .	33
7	Stress distribution across the cohesive zone (a) and equivalent nodal forces in the finite element mesh (b) . . . . .	34
8	Finite element nodes along the potential fracture line . . . . .	35
9	Cohesive crack configurations at the first (a) and $(l - k + 1)$ -th (b) crack growth increment . . . . .	36
10	Dimensionless load vs. deflection diagrams by varying the brittleness number $s_E, a_0/h = 0.0$ . . . . .	37
11	Decrease in apparent strength by increasing the specimen size . . . . .	38
12	Constant distribution of cohesive stresses . . . . .	39
13	Fictitious crack depth at the maximum load as a function of the specimen size . . . . .	40
14	Dimensionless load vs. deflection diagrams by varying the brittleness number $s_E, a_0/h = 0.5$ . . . . .	41
15	Increase of fictitious fracture toughness by increasing the specimen size . . . . .	42
16	A concrete specimen subjected to tension (a). Fractal localization of the stress upon the resistant cross section (b) and of the energy dissipation upon crack surface (c). . . . .	43
17	Fractal localization of the strain (a) and of the energy dissipation inside the damaged band (b). . . . .	44
18	Fractal cohesive model. . . . .	45
19	Tensile tests on dog-bone shaped concrete specimens (a) by Ferro [142]: stress-strain diagrams (b), cohesive law diagrams (c), fractal cohesive law diagrams (d). . . . .	46
20	Tensile strength (a) and fracture energy (b) vs. specimen size: experimental data by van Vliet [143] and linear interpolation in the bilogarithmic plot. . . . .	47
21	Tensile tests on dog-bone shaped concrete specimens (a) by van Vliet [143]: stress-strain diagrams (b), cohesive law diagrams (c), fractal cohesive law diagrams (d). The dashed lines refer to extrapolated values. . . . .	48
22	Details of the peak (a) and of the tail (c) of the cohesive law diagrams. Details of the peak (b) and of the tail (d) of the fractal cohesive law diagrams. The dashed lines refer to extrapolated values. . . . .	49
23	Direct tensile test on a concrete specimen (a) and fractal stress distribution over the resistant ligament (b). . . . .	50

24	Three point bending test concrete specimen (a) and fractal stress distribution over the resistant ligament (b). . . . .	51
25	The fractal bar subjected to an axial load: the displacement field. . . . .	52
26	Multifractal Scaling Laws for tensile strength and fracture energy. . . . .	53
27	Homogeneously diffused strain (a) and extremely localized deformation (b) along the bar, valid respectively for small and large structures. . . . .	54
28	Multifractal Scaling Law for the critical strain. . . . .	55

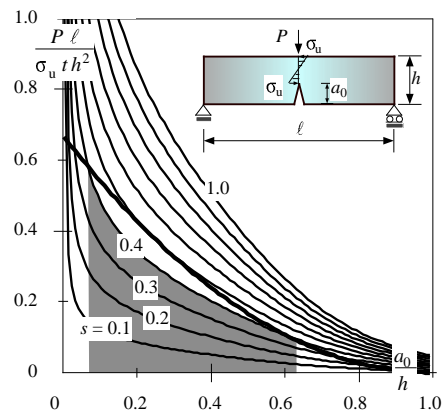


Figure 1: Dimensionless load of crack instability versus relative crack depth

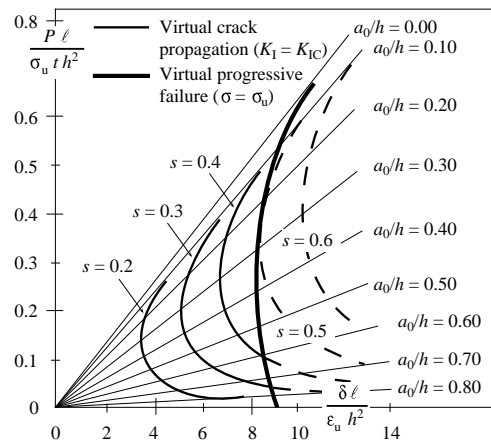


Figure 2: Dimensionless load of crack instability as a function of the dimensionless deflection

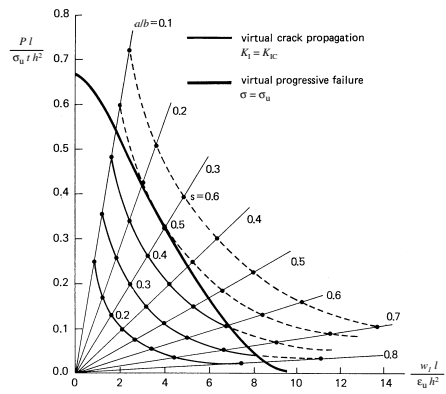


Figure 3: Dimensionless load of crack instability versus dimensionless crack mouth opening displacement

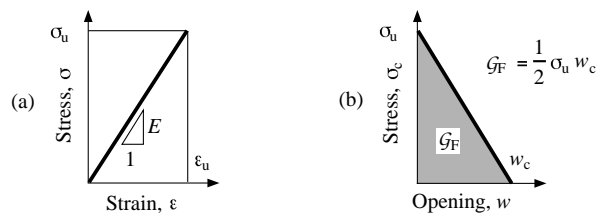


Figure 4: Constitutive laws of the cohesive crack model: (a) undamaged material, (b) process zone.

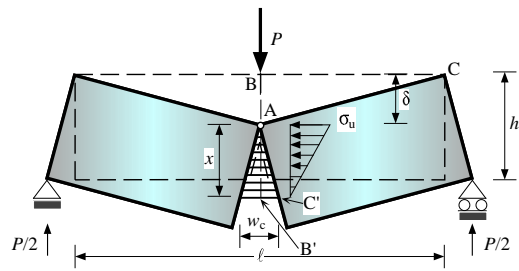


Figure 5: Limit-situation of complete fracture with cohesive forces

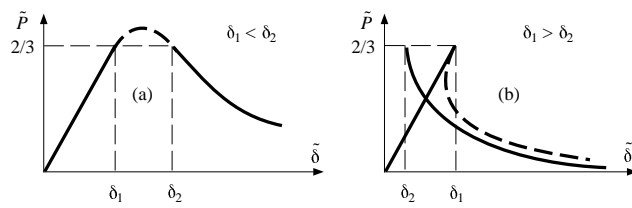


Figure 6: Load-deflection diagrams: (a) ductile and (b) brittle condition.

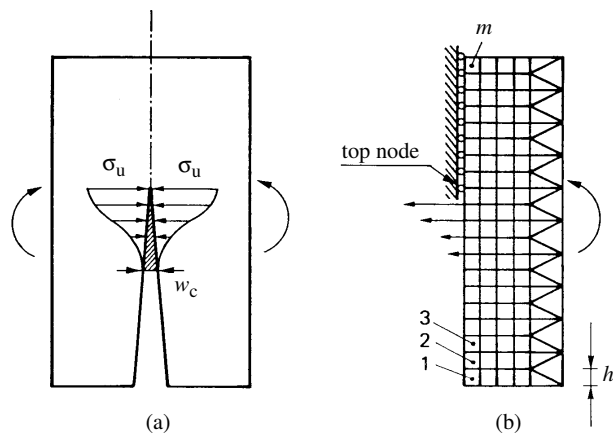


Figure 7: Stress distribution across the cohesive zone (a) and equivalent nodal forces in the finite element mesh (b)

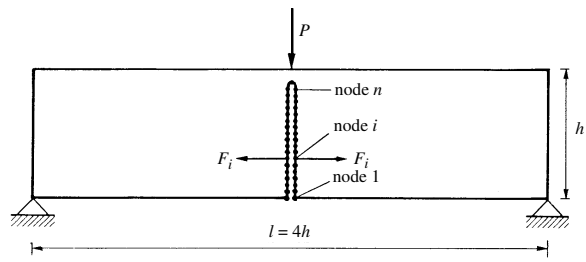


Figure 8: Finite element nodes along the potential fracture line

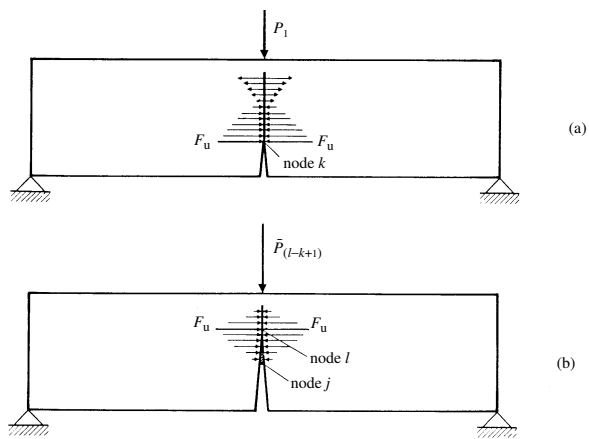


Figure 9: Cohesive crack configurations at the first (a) and  $(l - k + 1)$ -th (b) crack growth increment

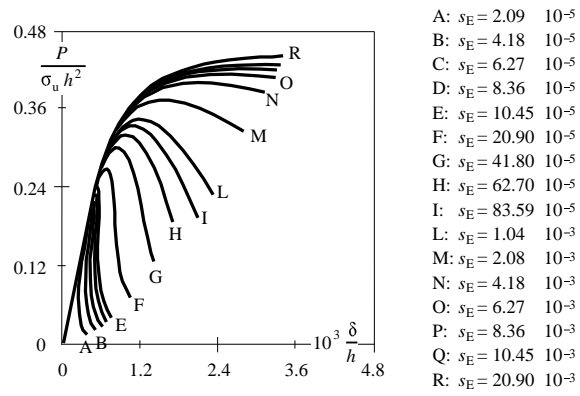


Figure 10: Dimensionless load vs. deflection diagrams by varying the brittleness number  $s_E$ ,  $a_0/h = 0.0$

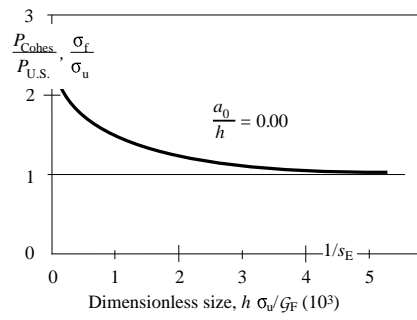


Figure 11: Decrease in apparent strength by increasing the specimen size

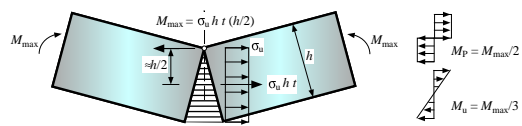


Figure 12: Constant distribution of cohesive stresses

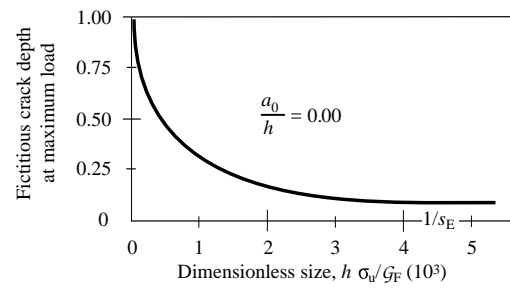


Figure 13: Fictitious crack depth at the maximum load as a function of the specimen size

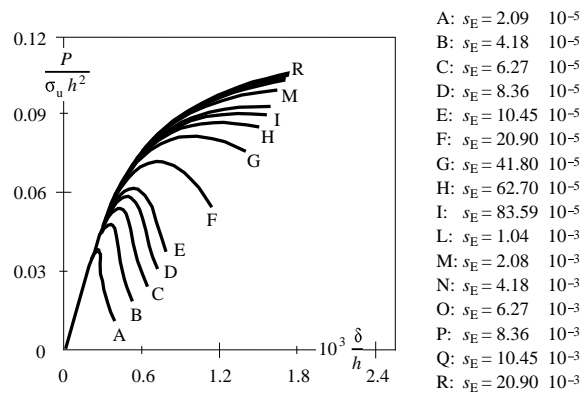


Figure 14: Dimensionless load vs. deflection diagrams by varying the brittleness number  $s_E$ ,  $a_0/h = 0.5$

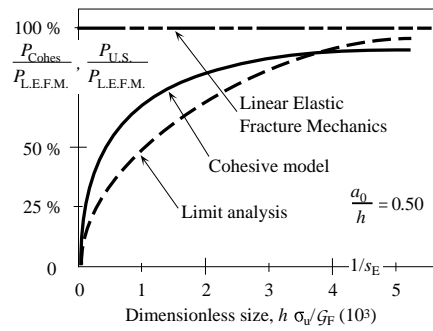


Figure 15: Increase of fictitious fracture toughness by increasing the specimen size

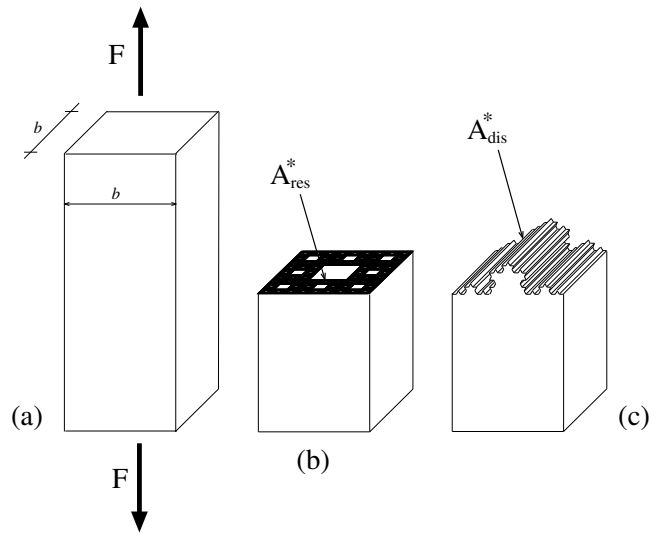


Figure 16: A concrete specimen subjected to tension (a). Fractal localization of the stress upon the resistant cross section (b) and of the energy dissipation upon crack surface (c).

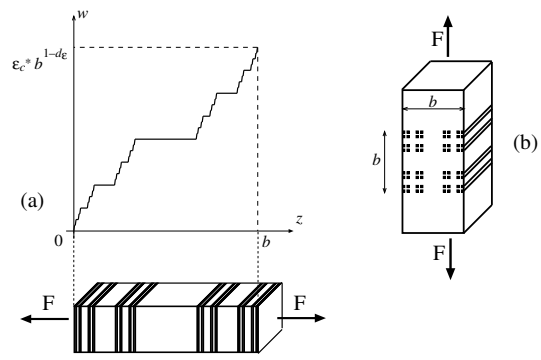


Figure 17: Fractal localization of the strain (a) and of the energy dissipation inside the damaged band (b).

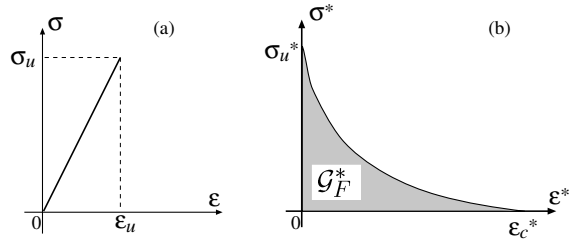


Figure 18: Fractal cohesive model.

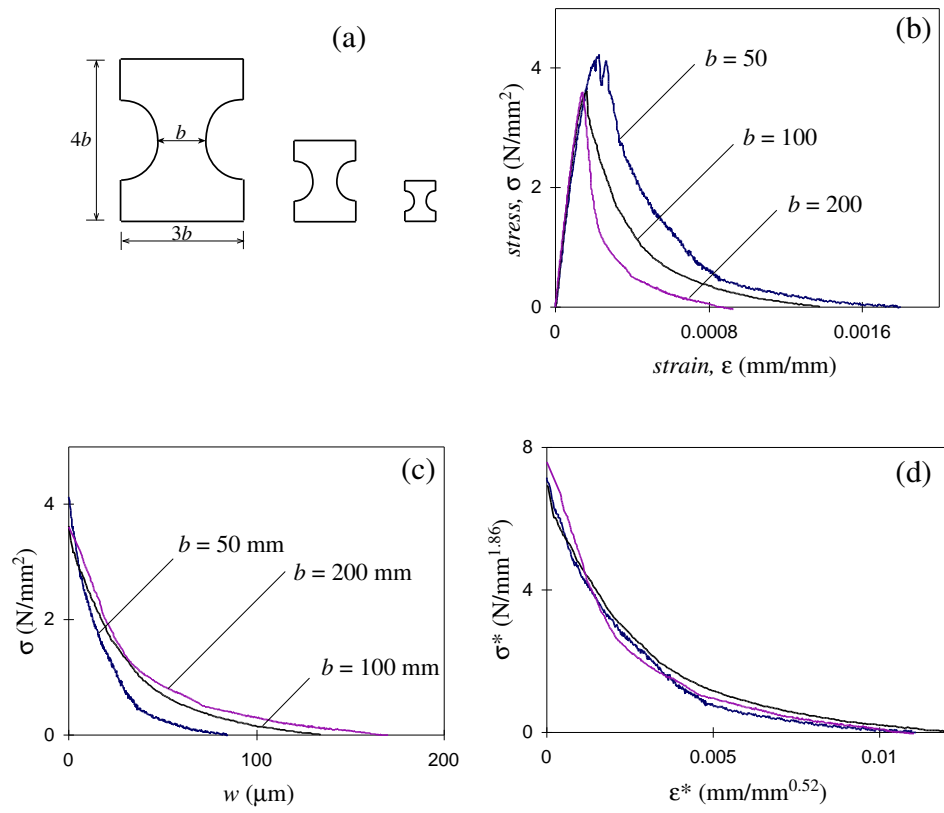


Figure 19: Tensile tests on dog-bone shaped concrete specimens (a) by Ferro [142]: stress-strain diagrams (b), cohesive law diagrams (c), fractal cohesive law diagrams (d).

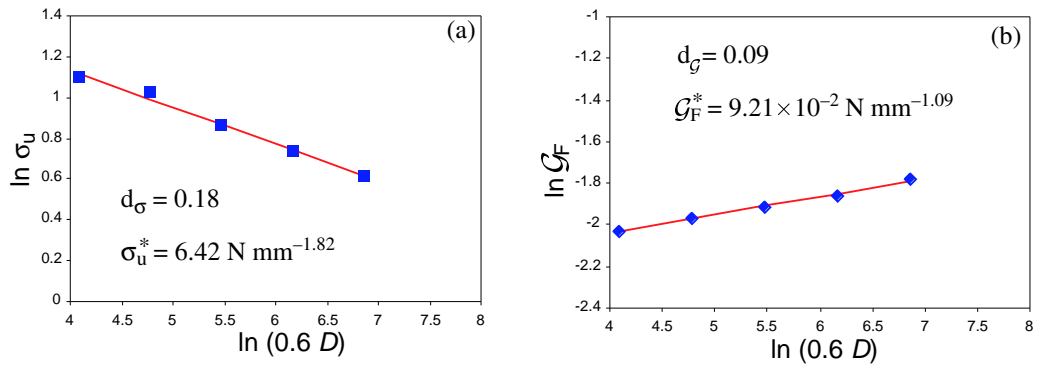


Figure 20: Tensile strength (a) and fracture energy (b) vs. specimen size: experimental data by van Vliet [143] and linear interpolation in the bilogarithmic plot.

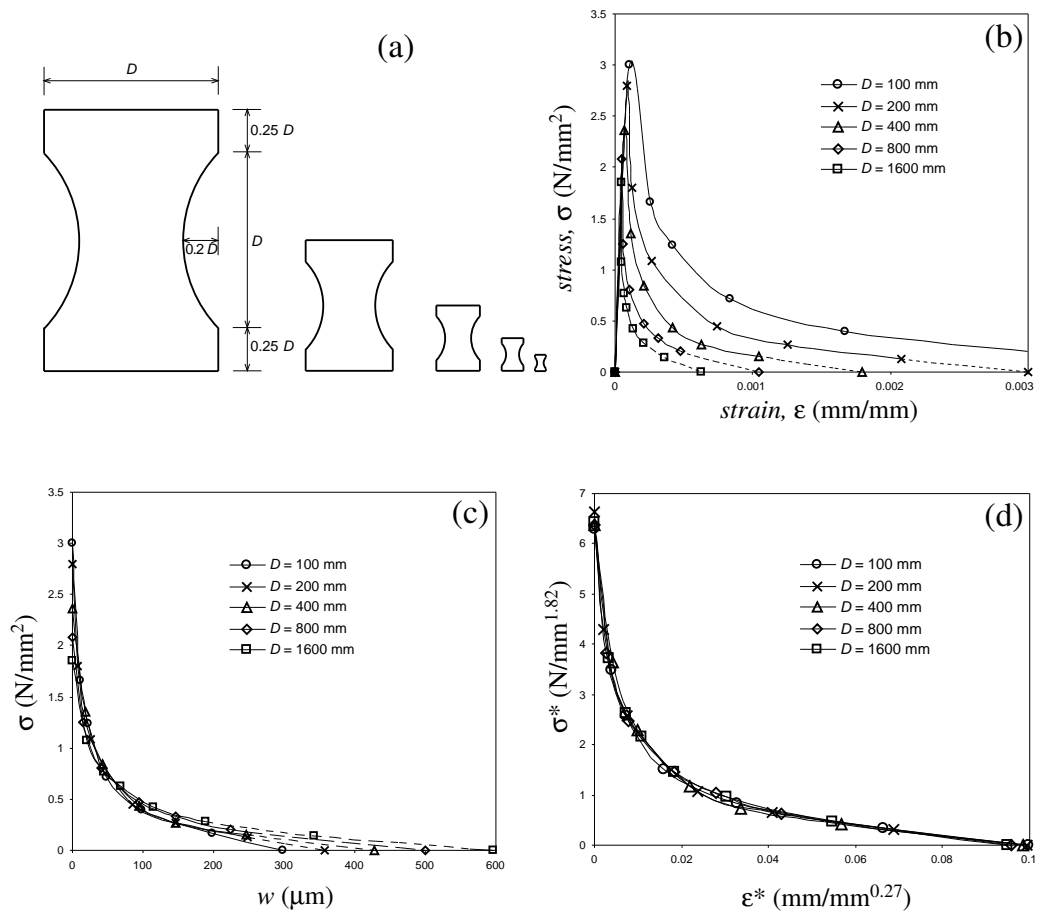


Figure 21: Tensile tests on dog-bone shaped concrete specimens (a) by van Vliet [143]: stress-strain diagrams (b), cohesive law diagrams (c), fractal cohesive law diagrams (d). The dashed lines refer to extrapolated values.

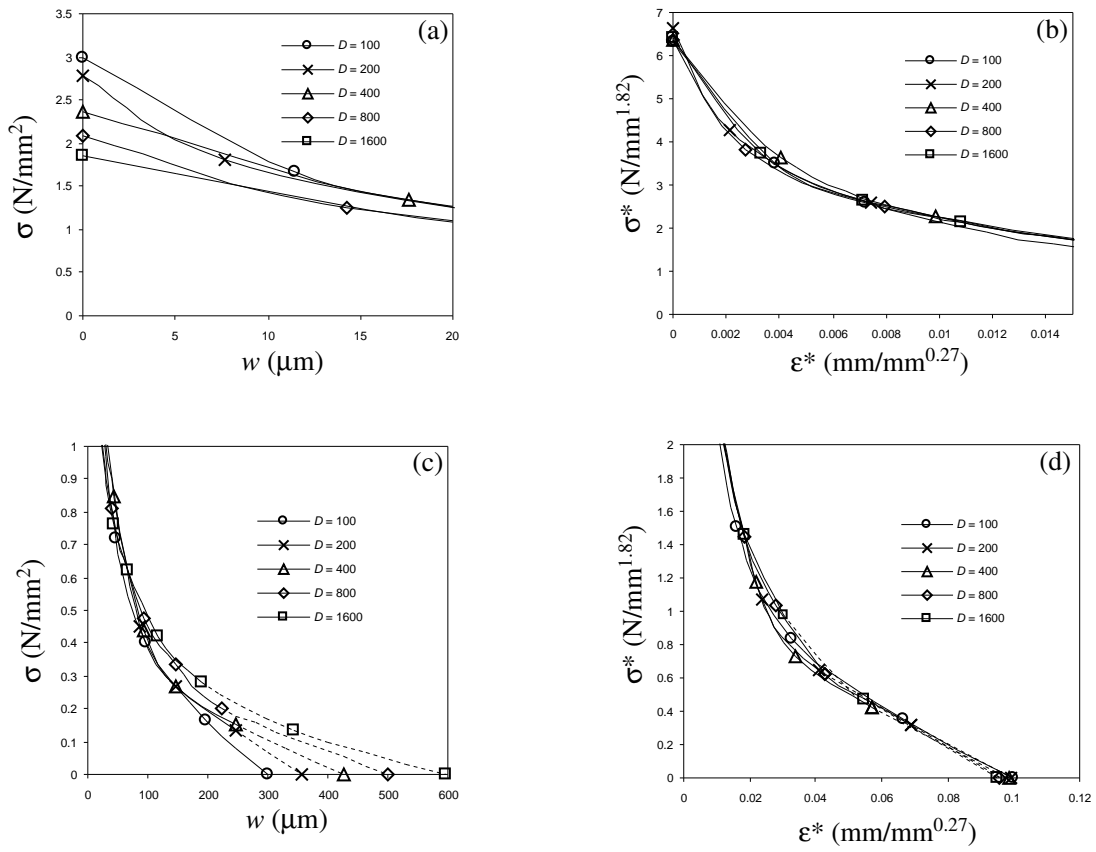


Figure 22: Details of the peak (a) and of the tail (c) of the cohesive law diagrams. Details of the peak (b) and of the tail (d) of the fractal cohesive law diagrams. The dashed lines refer to extrapolated values.

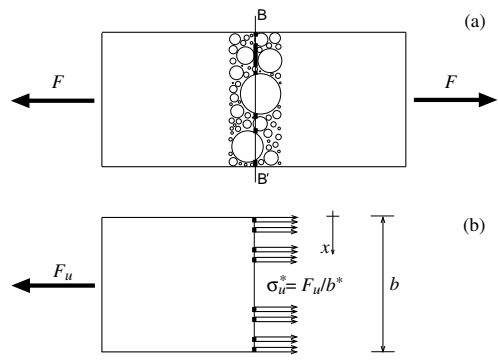


Figure 23: Direct tensile test on a concrete specimen (a) and fractal stress distribution over the resistant ligament (b).

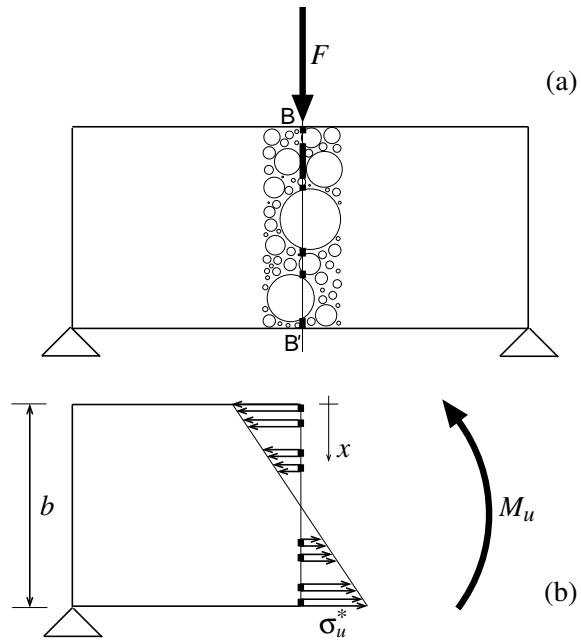


Figure 24: Three point bending test concrete specimen (a) and fractal stress distribution over the resistant ligament (b).

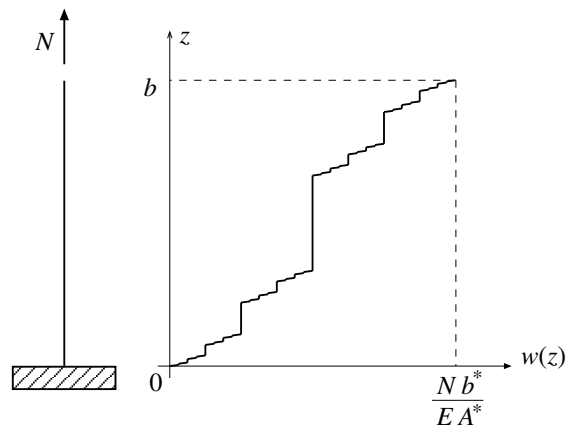


Figure 25: The fractal bar subjected to an axial load: the displacement field.

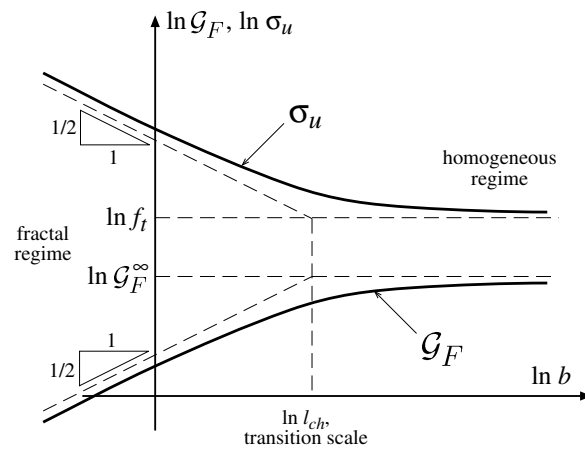


Figure 26: Multifractal Scaling Laws for tensile strength and fracture energy.

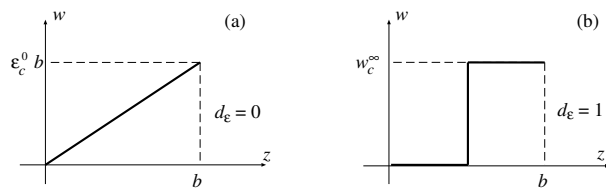


Figure 27: Homogeneously diffused strain (a) and extremely localized deformation (b) along the bar, valid respectively for small and large structures.

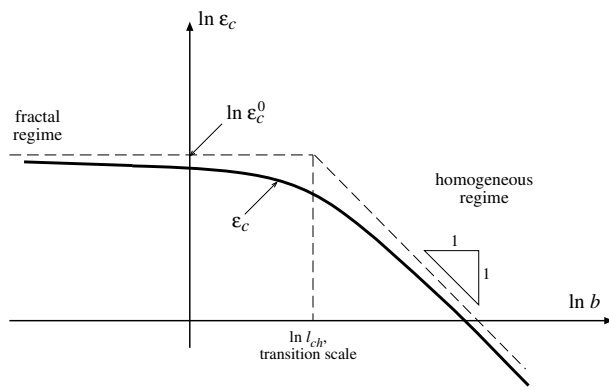


Figure 28: Multifractal Scaling Law for the critical strain.